Investigating the Impacts of Daytime Boundary Layer Clouds on Surface Energy Fluxes and Boundary Layer Structure During CHEESEHEAD19

J. Sedlar[1,2] ⓘ, L. D. Riihimaki[1,2] ⓘ, D. D. Turner[3] ⓘ, J. Duncan[1,4,5] ⓘ, B. Adler[1,4] ⓘ, L. Bianco[1,4] ⓘ, K. Lantz[2] ⓘ, J. Wilczak[4] ⓘ, E. Hall[1,2], C. Herrera[1,2] ⓘ, and Gary B. Hodges[1,2]

[1]Cooperative Institute for Research in Environmental Sciences, University of Colorado Boulder, Boulder, CO, USA, [2]NOAA Global Monitoring Laboratory, Boulder, CO, USA, [3]NOAA Global Systems Laboratory, Boulder, CO, USA, [4]NOAA Physical Sciences Laboratory, Boulder, CO, USA, [5]Now at WindESCo, Burlington, MA, USA

Abstract Studies of land-atmosphere interactions under a clear sky and low cumulus cloud conditions are common from long-term observatories like at the southern great plains. How well the relationships and responses of surface radiative and turbulent heat fluxes determined from these investigations hold for more heterogeneous surfaces in other climate regimes, however, is uncertain. In this study, detailed observations of the surface energy budget and daytime boundary layer properties are analyzed using measurements from the Chequamegon Heterogenous Ecosystem Energy-Balance Study Enabled by a High-Density Extensive Array of Detectors 2019 (CHEESEHEAD19) field campaign, July-October 2019, across a heterogeneous forested landscape of northern Wisconsin. A cloud regime framework is employed to classify consecutive periods of clear skies from lower atmosphere stratiform and cumulus clouds. A seasonal transition from low cumulus to low stratiform periods occurred, together with a diurnal pattern in cloudy or clear sky period dominance. Radiative forcing was highly dependent on sky conditions, leading to changes in the redistribution efficiency of radiative energy by the surface turbulent heat fluxes. During CHEESEHEAD19, small Bowen ratios dominated with daytime latent heat fluxes three times as large as sensible heat fluxes for all sky conditions studied; the forested region, therefore, falls within an energy-limited regime. The depth of the daytime mixed layer depended upon the sky condition and thermodynamic setting; deeper mixed layers occurred during periods of low cumulus and not clear skies. Profiles of vertical velocity were found to have enhanced variance under low cumulus compared to clear sky periods, suggesting potential for cloud feedbacks on boundary layer structure and surface energy fluxes.

Plain Language Summary This study investigates how different cloud regimes influence the exchange of energy at Earth's surface over a highly heterogeneous forested landscape in northern Wisconsin. Clouds directly modify the solar and infrared radiation reaching the surface. In turn, the modifications to radiation affect how turbulence near the surface is generated and its magnitude. The net result of these energy fluxes determines the warming and cooling processes at the surface, with direct implications on the development of local weather systems. From the observations in northern Wisconsin, an apparent partition in energy fluxes between two commonly observed lower atmosphere cloud types is found. A seasonal pattern in the occurrence of these cloud types was observed. Because of these cloud-specific preferences, turbulence generated near the surface was larger during the first half of the 3-month field campaign. Enhanced surface fluxes supported a deeper boundary layer for the shallow cumulus cloud conditions compared to overcast conditions. These fluxes were even larger than periods when skies were clear; however clear sky conditions were most frequent during the morning when surface energy fluxes were generally increasing with time during this development stage of the convective mixed layer. Turbulent fluxes associated with evaporation at the surface dominated over dry fluxes, regardless of the overhead sky conditions. These findings represent important differences to heavily study climatological regions where grasslands make up the primary surface characteristics.

1. Introduction

The transfer of energy through Earth's climate system is strongly influenced by the presence of clouds through their interactions with radiative transfer processes. The surface energy budget (SEB) response and the feedback

on the lower atmosphere cloud cover represents an important forcing term in the diurnal evolution of weather systems and the hydrological cycle, as well as on human health through the dispersion of trace gases, particles, and pollution. Boundary layer clouds are unique in that they evolve within a layer of the atmosphere that is in direct contact with the surface and therefore are influenced by turbulent mixing, thermodynamic evolution, vegetation properties, and moisture availability at, and even below, the surface. These low clouds can be advected laterally, can be driven locally through land-atmosphere (L-A) interactions, or through a combination of both forced and local processes (Zhang et al., 2017). Therefore, an improved understanding of important L-A interactions is crucial in characterizing the intimate relationship between different cloud types, the boundary layer structure, surface energy partitioning, and how these properties vary with different cloud types.

Traditionally, L-A interaction studies have focused on simplified situations that aim to reduce complexity in order to gain process-level knowledge. For example, diagnosis of boundary layer structures and turbulent characteristics observationally have often focused on clear sky conditions (e.g., Berg et al., 2017; McNicholas & Turner, 2014; Turner et al., 2014). Such studies frequently rely on remote sensing instruments that can retrieve vertical motion profiles and for some remote sensing measurements, clouds can inhibit retrievals such as with lidar backscatter. Across surfaces of forested or mixed forest and field, the horizontal variation in surface vegetation type and dynamic characteristics, such as surface roughness, can contribute to boundary layer cloud fields. Variability in surface properties results in partitioning differences of the surface energy fluxes, and the partitioning of fluxes may be critical for shallow cumulus cloud formation (e.g., Rabin et al., 1990). More recently, studies have explored boundary layer properties and L-A interactions when comparing and contrasting clear sky conditions with shallow, low cumulus cloud fields (e.g., Chandra et al., 2010; Fast et al., 2019; Tao et al., 2019). Other studies rely on finite-domain representations through numerical modelings such as high-resolution large eddy and cloud-resolving model simulations. A fair amount of consideration has been given to understanding daytime cloud evolution over the land, such as development and morphology, through model simulations (Brown et al., 2002; Zhang et al., 2017), as well as through observations characterizing the convective or turbulent environments leading to shallow cumulus cloud fields (Berg & Kassianov, 2008; Chandra et al., 2010; Lareau et al., 2018).

Numerical simulations of modeled fractional cloud cover were sensitive to the spatial variability of surface fluxes (Xiao et al., 2018; Zhong & Doran, 1997) since surface flux partitioning changes with surface characteristics, influencing surface-forced boundary layer cloud properties. However, models often have difficulty representing even the bulk macrophysical characteristics of cloud cover such as cloud fraction and cloud vertical partitioning. Clouds influence the radiative transfer at the surface, which alters the homogeneity of surface turbulent fluxes driving the daytime mixed layer. The time scale of surface fluxes influences the response of vertical velocity variance within the mixed layer (van Driel & Jonker, 2011). In turn, variability in vertical motion alters the updraft and downdraft characteristics and can impact cloud evolution. Once clouds are present, cloud shielding of radiation can influence the amount of surface energy partitioning through changes in the surface temperature, which will affect both the sensible and latent heat flux (Rieck et al., 2014). In turn, feedback may emerge where the vertical growth of the boundary layer may be influenced by the radiative forcing of the cloud and its influence on the redistribution of turbulent heat fluxes (Golaz et al., 2001).

Sensitivity studies from various land surface models (LSMs) and planetary boundary layer (PBL) schemes in the Weather Research and Forecasting (WRF) numerical weather prediction model revealed that surface fluxes had a strong control on the boundary layer development. LSM-produced surface fluxes exerted more sensitivity on boundary layer evolution than the PBL schemes that were tested (Milovac et al., 2016); surface fluxes experienced far greater sensitivity to the choice of LSM compared to the PBL scheme, and the modeled turbulent heat fluxes near the top of the boundary layer had a larger sensitivity to the LSM choice than the PBL scheme. Ek and Holtslag (2004) also developed a connection between relative humidity tendency at the top of the PBL with boundary layer cloud formation that depended in part on the availability of soil moisture, further highlighting the importance of L-A interactions. These results imply that an improved understanding of how the SEB components and boundary layer depth respond to surface turbulent heat fluxes under different sky conditions is warranted.

Less attention has been placed on the observed SEB response and partitioning of turbulent fluxes and boundary layer depth properties for different sky conditions, such as during overcast, low stratiform cloud cover, broken low cumulus, and clear skies. This is especially true over heterogeneous terrain. The Local Coupling, or LoCo, the framework to characterize and understand L-A interactions identified the importance of ground, surface, and near-surface moisture and thermodynamic states to diagnose the development of the coupled L-A interactions
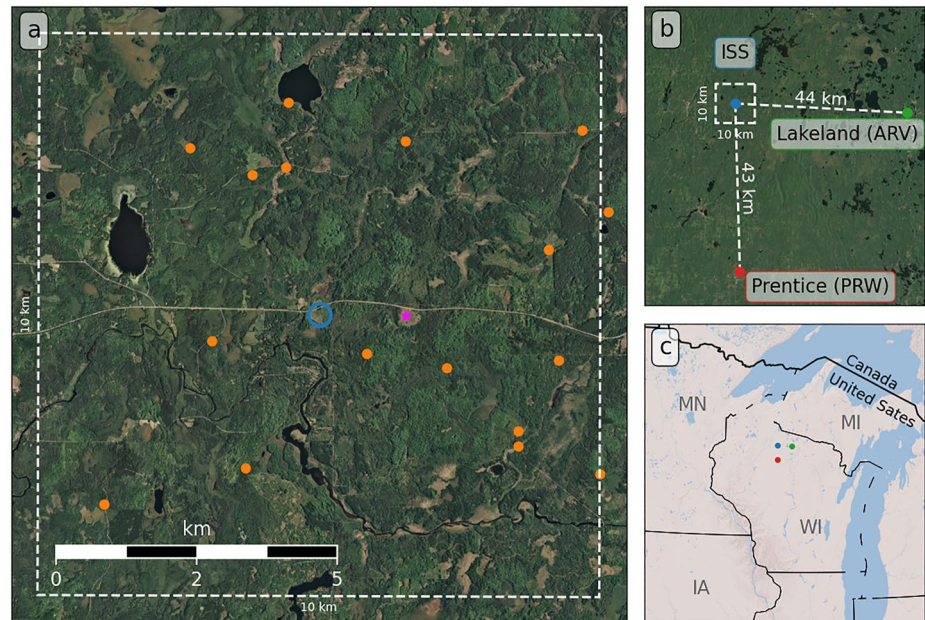
Figure 1. Spatial distributions of surface observations stations during Chequamegon Heterogenous Ecosystem Energy-Balance Study Enabled by a High-Density Extensive Array of Detectors 2019 (CHEESEHEAD19). (a) 10 × 10 km domain (white dashed border) encompassing the 17 National Center for Atmospheric Research Integrated Surface Flux Stations station locations (orange filled circles), the main ISS observatory (blue circle), and the WLEF tall tower observatory (magenta star). (b) Locations of Lakeland (ARV, green circle) and Prentice (PRW, red circle) observatories in relation to the main domain in (a). (c) Regional view of the main observatories of CHEESEHEAD19.

(Santanello et al., 2011). However, the lack of routine observations of cloud interactions in the L-A framework remains elusive, further inhibiting fundamental understanding of the feedback within the boundary layer system (Santanello et al., 2018). Fitzjarrald and Moore (1994) and Freedman et al. (2001) have demonstrated how seasonal transitioning of vegetation characteristics of a woodland site can influence the partitioning of surface fluxes and mixed layer thermodynamics. Ultimately, the ability of the land surface to force the local development of boundary layer clouds is contingent upon a number of interconnected processes (e.g., Freedman et al., 2001). The response of the surface fluxes to boundary layer clouds may result in feedback between L-A interactions.

This study aims to improve understanding of the SEB and boundary layer responses to lower atmosphere boundary layer clouds and clear sky periods over heterogeneous surfaces, using observations collected in northern Wisconsin. Measurements from the Chequamegon Heterogenous Ecosystem Energy-Balance Study Enabled by a High-Density Extensive Array of Detectors 2019 (CHEESEHEAD19) intensive, heavily instrumented field campaign over a relatively small observational domain during July through early October 2019 (Butterworth et al., 2021) provide the observational framework for this study. Sky conditions are separated by consecutive, lower atmosphere boundary layer cloud regimes and clear sky periods using a novel cloud classification framework. The field observations and analysis methods are described in the next section. Results examining the SEB partitioning and boundary layer height properties separated by sky condition, including analysis of boundary layer vertical velocity characteristics, follow in subsequent sections.

2. Data and Methodology

The CHEESEHEAD19 observational field campaign took place in the Chequamegon-Nicolet National Forest near Park Falls, WI (45.95°N, 90.27°W; Figure 1). Measurements commenced during late June 2019 and measured continuously through early October 2019, capturing the seasonal transition of summer into autumn. This northern Wisconsin ecosystem consists of heterogeneous forested terrain interspersed with open grassland and various vegetation types and water bodies. Overarching experiment goals included "(a) to investigate causes of energy balance non-closure over heterogeneous ecosystems and (b) to address the problem of scaling surface energy fluxes" (Butterworth et al., 2021). To address the experiment goals, a square 10 × 10 km domain

was established around heterogeneous surfaces and was heavily instrumented with surface-based sensors, towers, and remote sensing instrumentation (Figure 1a). These systems included meteorology and surface energy fluxes, in situ and remotely sensed atmospheric profilers and airborne observations. Butterworth et al. (2021) describe in detail the observational systems and measurement principles deployed during CHEESEHEAD19.

2.1. Study Region

A total of 17 Integrated Surface Flux Stations (ISFS) operated by the National Center for Atmospheric Research-Earth Observing Laboratory (NCAR-EOL) were deployed within the 10 × 10 km CHEESEHEAD19 domain amongst different land-use types including forest, open field, complex/variable surface vegetation, and varying surface water saturation characteristics (Butterworth et al., 2021). The location of each ISFS within the domain is shown in Figure 1a. Each station was equipped with broadband radiometers to measure net radiation, a sonic anemometer for high-frequency temperature and 3D winds, a LICOR gas hygrometer for high frequency.

Water vapor variations, ground heat fluxes, and volumetric soil moisture measurements, and general meteorology. All but four sonics and LICOR paired sensors were mounted near the top of the masts at each station between 25 and 30 m AGL above the local canopy, the others ranged 2–10 m AGL; ground heat and moisture measurements were made in the 0–5 cm depth below the surface. Turbulent heat and momentum fluxes were calculated by the eddy covariance technique by NCAR's processing methodology (see https://www.eol.ucar.edu/content/corrections-sensible-and-latent-heat-flux-measurements).

In the approximate center of the CHEESEHEAD19 study area, two supersites were established and an extensive suite of passive and active remote sensing instruments was colocated. These stations are the Integrated Sounding Suite (ISS) and the WLEF 400 m tall tower sites (Figure 1a); the latter has been an operational Ameriflux tower site for some time (Andrews et al., 2014) and therefore was a natural anchorpoint for additional campaign measurements. The ISS site was approximately 1.6 km west of WLEF in an open field surrounded by forest. Here, NOAA-GML operated a Mobile SURFRAD station in the east-central ISS field, measuring high-quality direct and diffuse solar components and broadband up- and downwelling radiation. These detailed radiation measurements, in particular the solar components, are needed in order to process the measurements through the Radiative Flux Analysis, or RadFlux, processing and retrieval suite (Long & Ackerman, 2000; Long et al., 2006; Long & Turner, 2008). Mobile SURFRAD was designed to operate under the same measurement philosophy as the long-duration, 25+ years, SURFRAD network (Augustine et al., 2000), but instead for short-term deployments. Complementing the radiation measurements, the Mobile SURFRAD station contains a Total Sky Imager, capturing sub-minute hemispheric sky images, and a Vaisala CL51 ceilometer for automated retrievals of cloud presence, cloud base height, and boundary layer height.

Two additional sites, each approximately 45 km away from the 10 × 10 km CHEESEHEAD19 domain, were established at the Lakeland (east) and Prentice (south) Airports (Figure 1b). NOAA-GML deployed two radiation and cloud observation stations that were slightly less comprehensive than the Mobile SURFRAD at ISS. These stations measured only the downwelling radiative flux components, although the stations contain the required measurements necessary to produce radiation and cloud data products using RadFlux processing retrievals. Each station also contained a Vaisala CL51 ceilometer for cloud and boundary layer height estimates. Additionally, NOAA-PSL deployed a 915 MHz wind profiling radar at each airport. A fuzzy logic algorithm (Bianco et al., 2008) incorporates radar wind profiler (RWP) vertical profiles of signal-to-noise ratio, vertical velocity variance, and spectral width of the vertical velocity to estimate the daytime mixed layer height. No surface-based turbulent measurements were made at these sites. A Dopper lidar was installed near the base of the tall WLEF tower, directly east of the ISS site. Vertical stares by the lidar provide profiles of vertical velocity, which are examined at various normalized levels within the daytime mixed layer.

2.2. Surface Energy Budget

To analyze the surface energy budget response to boundary layer clouds, all surface energy flux and surface meteorological datasets are averaged onto a 30 min time resolution. The average radiative fluxes are computed from the data within 15 min of each averaging period. Turbulent sensible heat flux (H_s) and latent heat flux (H_l) are averaged by taking the two 30 min values on either side of the averaging period in order to account for lag (hysteresis) from the radiative fluxes (i.e., Kivalov & Fitzjarrald, 2019). Temporal averages of turbulent heat

fluxes (THFs) and ground fluxes were also spatially averaged across all 17 flux stations to avoid local vegetation, phenology, and canopy characteristics biasing the analysis toward a particular measurement site. Net surface radiation from the ISS Mobile SURFRAD was compared to spatially-averaged net radiation from all 17 ISFS stations for the full CHEESEHEAD19 campaign. A close relationship ($r^2 = 0.98$) and a small mean bias (-17 W m^{-2}) were striking (not shown). This close agreement lends confidence that the radiative fluxes were generally homogeneous over the 10×10 km^2 domain, suggesting that similar sky and cloud conditions were common across the study area. This lends support to focus our analysis on the ISS site radiative fluxes, which is advantageous as the RadFlux value-added products, TSI images, and PBL height observations are also available at the ISS site. All analyses below use the 30 min averaged observations, except for the high-frequency vertical velocity profile data from the Doppler lidar.

2.3. Low Cloud Regime Separation

Periods of boundary layer clouds are classified using the cloud type model described by Sedlar et al. (2021), a random forest machine learning model trained and evaluated from years of daytime observations. The inputs, also called features, for this random forest classifier model include high-quality surface radiation and cloud products derived from RadFlux. Hemispheric sky cover fraction, cloud radiative effect, and moving standard deviation of shortwave transmissivity are examples of value-added RadFlux data product ingested as features into the random forest cloud classifier; cloud presence and cloud base height from ceilometer observations are the only input feature not derived from radiative products. The cloud type model accuracy was reported around 75%–80% from independent evaluations (Sedlar et al., 2021). Further, sufficient training of the cloud type model led to a robust separation between low stratiform and low cumulus clouds, especially when considering the radiative impact of these very different boundary layer cloud types. Because RadFlux data processing and products are needed as input for the classifier, cloud type is only produced where NOAA-GML observations were collected: namely, at the ISS, Lakeland, and Prentice sites.

3. Results

3.1. Boundary Layer Clouds

Daytime cloud types were classified at ISS, Lakeland, and Prentice using the radiation and cloud property input features described in Sedlar et al. (2021). The clouds of interest in this study are considered low boundary layer clouds due to their cloud base height above the surface, which typically ranged from a few hundred meters up to 2 km (not shown); as will be shown later, the daytime mixed layer height was frequently of the same height range and therefore at least one boundary of these clouds was within the boundary layer. Because the cloud type relies on solar radiation measurements, cloud classification is limited to times when the solar zenith angle is less than 80°, nominally between 06:00-18:00 LST during CHEESEHEAD19. The cloud classification model produces a cloud type every 1 min which inherently introduces a variance, or jumpiness, between classified cloud types; this is especially true for low stratiform and low cumulus clouds. Based on their similarity in surface radiative signatures, low stratiform cloud scenes have a tendency to be misclassified as multi-layered low-high clouds, while shallow cumulus can be classified as a clear sky or high cirrus (Sedlar et al., 2021). The 1-min cloud types were post-processed to identify periods of consistent low stratiform and low cumulus cloud regimes by checking the temporal variance for frequent misclassifications within a 5 min window. If the sky cover fraction and cloud base heights of misclassifications within the 5-min period were consistent with the "true" cloud type, these classifications were relabeled as either a low stratiform or low cumulus cloud scene. Relating the estimated lifting condensation level (LCL) with cloud base height can also aid in identifying boundary layer clouds coupled to the surface (e.g., Freedman et al., 2001).

From the post-processed low boundary layer cloud classifications, consecutive cloud periods persisting for at least 2 hr were identified; their occurrence frequency by month is shown in Figures (2a–2c). Low cumulus clouds (red bars) were most common during the first half of the campaign, with July and August ranging from 17 to 22 periods of more than 2 consecutive hours of low cumulus periods. An abrupt transition occurred in September, with fewer than 8 consecutive cumulus periods, and almost no cumulus in October. Similar seasonal cumulus transitions have been observed in other forested regions and are responsive to changes in surface flux partitioning through seasonal vegetation characteristics (Fitzjarrald & Moore, 1994; Freedman et al., 2001). An
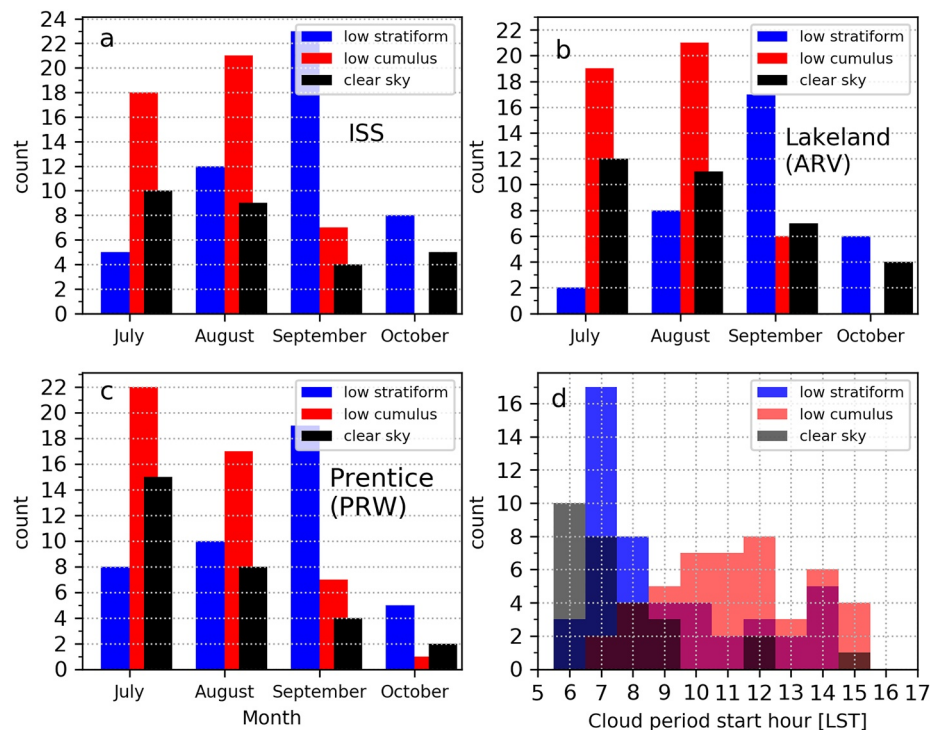
Figure 2. Distributions (counts) of at least 2 hr consecutive periods of a particular cloud type at (a) ISS, (b) Lakeland Airport (ARV), and (c) Prentice Airport (PRW). (d) Distributions of consecutive cloud period start time (hour in local standard time, LST) at integrated sounding suite. Colors represent the three sky conditions: low stratiform (blue), low cumulus (red), and clear sky (black).

opposite trend in the periods of low stratiform (blue bars) is evident, with the fewest periods in July and an increasing occurrence during the transition from late summer to early autumn. CHEESEHEAD19 concluded on 11 October which is reflected in the low number of occurrences of consecutive cloud periods for that month. The occurrence of clear sky periods greater than 2 consecutive hours was also identified (black bars), having a qualitatively similar seasonal transition as low cumulus. The similarity between seasonal trends and occurrence numbers of low cloud types amongst the three locations is encouraging and suggests quasi-homogeneous mesoscale forcing and subsequently sky conditions across the study region.

In addition to seasonal differences in low cloud occurrences, the onset of consecutive cloud periods exhibited a diurnal preference. Focusing on cloud types at the ISS site, periods of low stratiform clouds most frequently initiated during the early morning hours, their onset tapering off during the mid-morning (Figure 2d). Consecutive low stratiform clouds may have been present prior to the 07:00-08:00 LST peak start time but were not identified because of the daytime solar zenith angle restriction imposed. Low cumulus periods were observed increasingly later toward mid-morning and midday. Later onset time for cumulus is consistent with the generation and development of thermal plumes as solar radiation increases through the morning. Without additional moisture input to the growing mixed layer, the LCL will continue to increase more rapidly compared to the growing boundary layer, suppressing the onset of cumulus cloud fields (Haiden, 1997). Clear sky periods were primarily observed during the early morning with nearly 80% of >2 hr consecutive clear sky periods beginning before 09:00 LST. Distributions of cloud period start times at Lakeland and Prentice airports were similar to those at ISS and therefore are not shown.

Figure 3 shows the temporally varying occurrence of cloud periods together with the time series of surface energy fluxes and near-surface meteorological variables. A seasonal shift is evident in several of the meteorological parameters. The change from predominantly low cumulus periods to predominantly low stratiform periods happens around mid to late August (Figure 3a), as was seen in the total period numbers (Figure 2). Increasing solar zenith angles (lower solar elevations) from mid-summer to mid-autumn led to a reduction in net radiation (Figure 3b). Subsequently, the latent (H_l) and sensible (H_s) turbulent heat fluxes decline with the drop in available
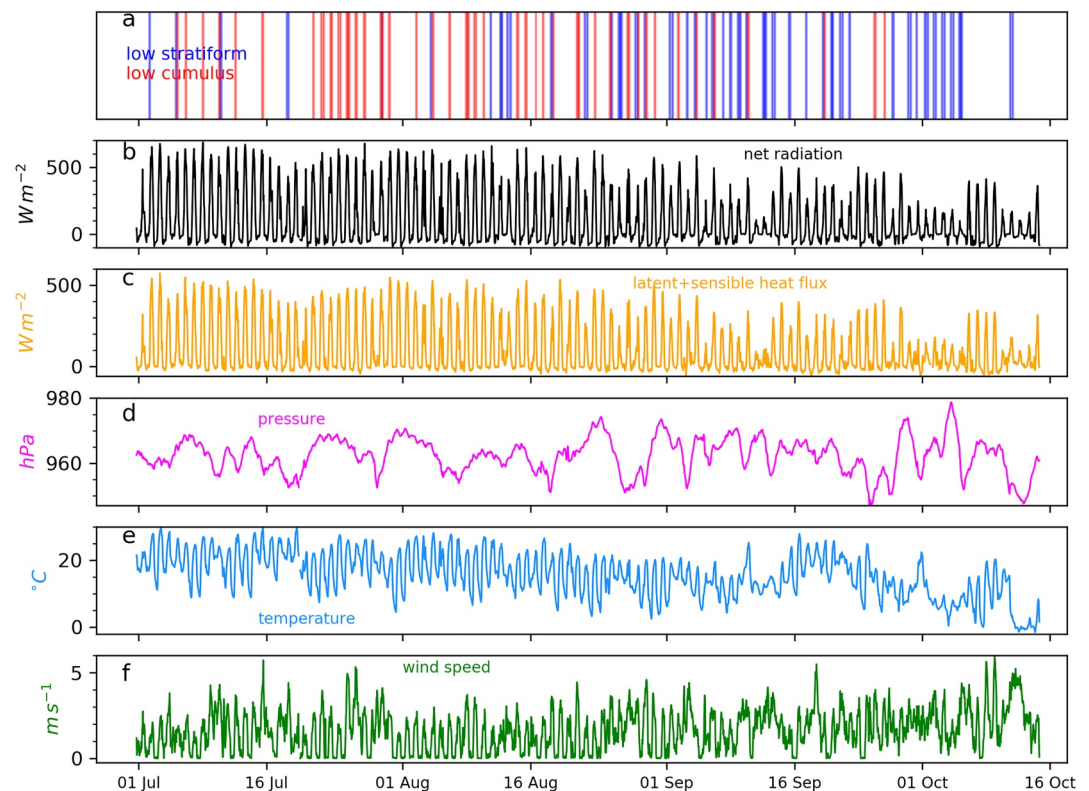
Figure 3. Time series showing the (a) start times of low stratiform (blue) and low cumulus (red) cloud periods, and 1 hr means of: (b) net surface radiation [W m^{-2}]; (c) latent and sensible heat flux [W m^{-2}]; (d) surface pressure [hPa]; (e) near-surface temperature [C]; and (f) 10 m wind speed [m s^{-1}].

net radiative energy (Figure 3c). Corresponding Bowen ratios (B = H_s/H_l) increased from summer to autumn in connection with a transition of canopy senescence and evapotranspiration efficiency (Butterworth et al., 2021). Decreasing net radiation at the surface led to a general declining trend in near-surface temperature, although some variability remained (Figure 3e). Surface pressure suggests the second half of the campaign experienced the more frequent occurrence of pressure changes than the first half (Figure 3d); while peaks and valleys in pressure were also evident through mid-August, the frequency with which they oscillated became higher (more frequent pressure changes) from September onwards. Generally, near-surface wind speeds remained similar, although the minimum winds speeds were generally higher over the latter half of the campaign than during the first half (Figure 3f).

Relative frequency distributions (RFDs) of the near-surface meteorological conditions during the clear sky, low stratiform, and low cumulus conditions are also considered. The largest differences between the two boundary layer cloud periods are seen in the near-surface thermodynamics. Near-surface temperatures were typically 5°C to 10°C warmer for low cumulus compared to low stratiform periods (Figure 4a). Analogously, relative humidity (RH) was considerably larger during the low stratiform periods, where RH rarely exceeded 70% during periods of low cumulus (Figure 4b). The general distributions for specific humidity (Figure 4c) were moderately similar between the two cloud types, indicating that systematic changes to absolute humidity between cloud types were not responsible for the large differences found in relative humidity; instead, the considerably cooler air temperatures were responsible for larger RH during low stratiform periods. Both near-surface pressure and wind speeds (Figures 4d and 4e) show modest differences in the distributions between the two cloud types. However, in terms of wind direction (Figure 4f) low stratiform clouds generally occurred when an easterly wind component was present, a feature essentially absent from the low cumulus cases; the low cumulus wind direction RFD showed predominant distribution peaks from the southwest and northwest. Differences in advected air mass origin likely contributed to the temperature differences between the two low cloud periods. The RFDs for clear periods (black) generally resembled the distributions during low cumulus. The most obvious differences
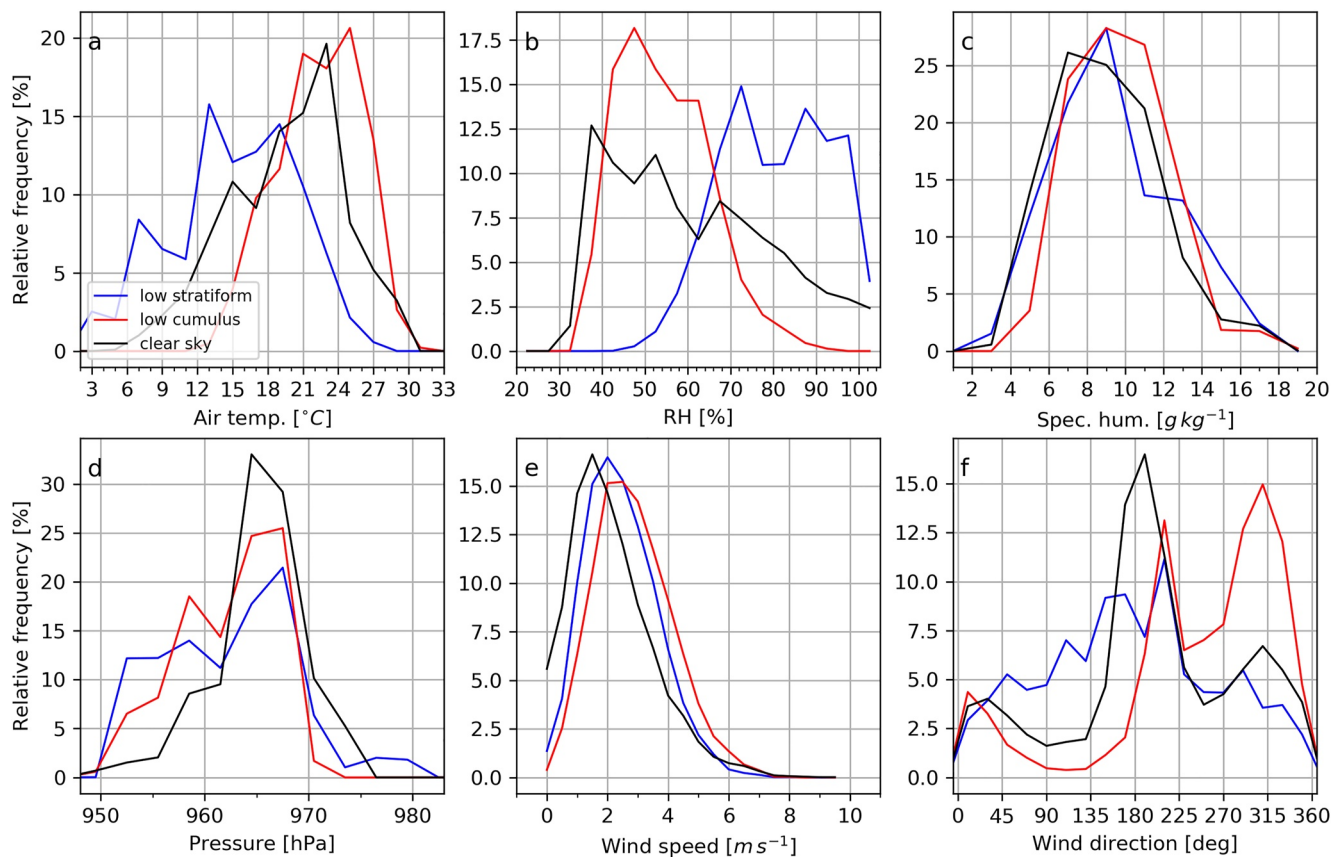
Figure 4. Relative frequency distributions of select near-surface meteorological parameters at the integrating sounding suite site, shown for each of the three sky conditions (colors): (a) air temperature [C]; (b) relative humidity (RH, [%]); (c) specific humidity [g kg⁻¹]; (d) surface pressure [hPa]; (e) wind speed [m s⁻¹]; and (f) wind direction [degrees].
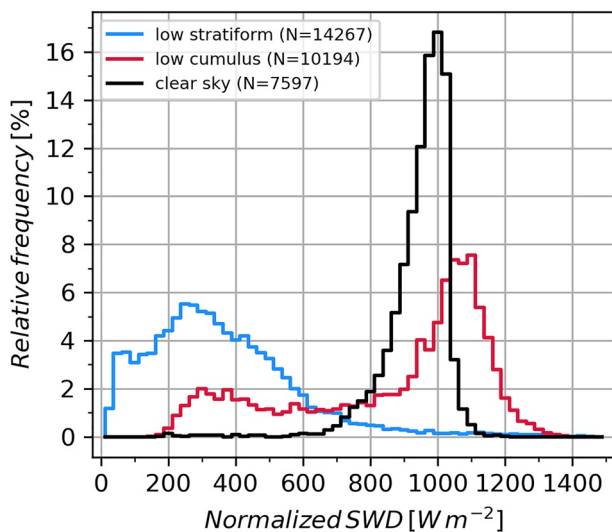

Figure 5. Relative frequency distributions of 1-min normalized downwelling shortwave ($\mu^{-1} \cdot$SWD [W m⁻²]) were observed during a consecutive cloud period. μ is the cosine of the solar zenith angle, and N in the legend is the number of 1-min observations within each consecutive cloud period.

in meteorology between clear and cumulus periods were observed for near surface winds, as well as a persistent surface pressure distribution toward slightly higher pressure. Lower wind speeds and higher pressure suggest that clear sky periods occurred during more quiescent conditions compared to the low cloud periods.

To highlight the impact boundary layer clouds impose on incoming radiation, Figure 5 shows RFDs of normalized shortwave downwelling (SWD) radiation measured at ISS for >2 hr consecutive cloud periods; to account for diurnal differences in cloud types, SWD is normalized by the cosine of solar zenith angle. SWD is strongly limited under low stratiform (blue) because of the characteristic overcast nature of these clouds; a dominant distribution peak between 200 and 400 W m⁻² emerges and is predominantly diffuse solar radiation. Shortwave radiation during low cumulus periods is systematically different from low stratiform. The SWD distribution has a bimodal structure, a primary mode at large values above 1000 W m⁻² and a secondary, smaller mode near 300 W m⁻² (red). The broken cloud fields typically associated with low cumulus cause this bimodal distribution, where the larger peak is associated with cloud-free, unshaded direct beam solar radiation and the smaller peak with fully attenuated direct-beam, leading to an SWD mode similar in magnitude to the diffuse-dominated low stratiform clouds (i.e., Kivalov & Fitzjarrald, 2019). The clear sky RFD typically ranges between 900 and 1000 W m⁻² (black). Interestingly, the maximum values of SWD
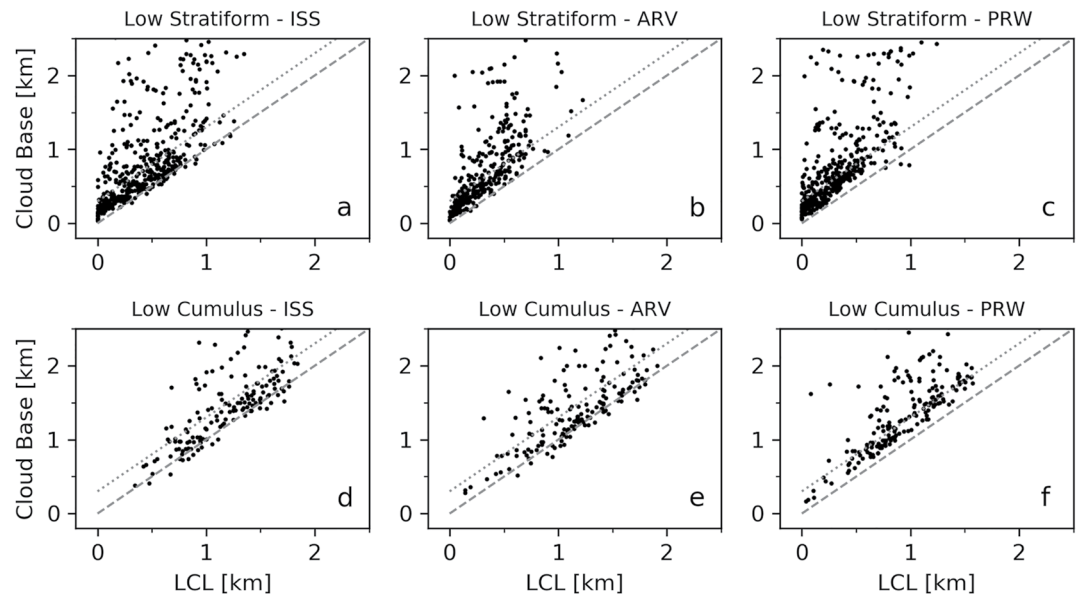
Figure 6. Scatterplots of ceilometer cloud base height [km] against lifting condensation level [km] during (top row) low stratiform and (bottom row) low cumulus cloudy periods. Subpanels represent scatterplots for the three stations: (a), (d) integrating sounding suite (b), (e) ARV, and (c), (f) PRW.

were higher during low cumulus periods than they were under clear sky conditions. This positive cloud effect is commonly seen in surface irradiance measurements in broken cloud fields when the direct normal irradiance reaches the sensor along with a higher diffuse irradiance than under clear skies due to the scattering from the cloudy portions of the sky. This effect is only captured in radiative transfer models that include 3D radiative effects and are not based on the Plane Parallel assumption (e.g., Gristey et al., 2020).

The differences seen in the SWD distributions indicate the random forest cloud classification model is successful in separating the two predominant boundary layer cloud regimes, in addition to clear sky periods. Furthermore, the amount of radiative energy reaching the surface is directly affected by the overlying sky conditions, especially when considering the seasonal transition of these boundary layer cloud regimes shown in Figures (2a–2c).

The relationship between low-level cloud and the lifting condensation level (LCL) is shown in Figure 6. A close connection between cloud base height and LCL height is indicative of whether the clouds are coupled with the surface or not likely to be influenced by surface forcing (Freedman et al., 2001). The relationship between LCL and cloud base for low stratiform (Fig. CBLCL a-c) and low cumulus (Figures 6d–6f) at the ISS, ARV, and PRW sites were typically well correlated; the majority of 30 min observed cloud base heights fell within 300 m of the derived LCL height. This relationship highlights a plausible coupling connection between the land surface and lower atmosphere (Fitzjarrald & Moore, 1994) during most of the observed low cloud regime periods. The cloud base-LCL connections during low stratiform periods at all three sites were more scattered compared to low cumulus periods, where cloud base height was considerably higher than the LCL; these cases represent periods where the cloud is likely not driven by land-atmosphere interactions.

Differences in the cloud base and LCL heights for the two cloud types are also evident; both heights were systematically lower for low stratiform periods. Increases in water vapor content near the surface and within the mixed layer can lower the height of LCL (Fitzjarrald & Moore, 1994; Haiden, 1997). While PDFs of surface specific humidity were generally similar amongst the sky conditions, relative humidity was much larger during the low stratiform periods (Figures 4b and 4c). How the LCL varied spatially, or lack of spatial variability, between ISS, ARV, and PRW is shown in Figure 7. The observations were stratified by the sky conditions observed at ISS: (a) low stratiform, (b) low cumulus, and (c) clear sky. The y-axis shows the LCLs at ARV (green) and PRW (purple) compared with LCLs at ISS (x-axis) for the different cloud types observed at ISS. A few interesting features relative to sky condition and location are revealed. First, as indicated in Figure 6, the cloud regimes correspond to different LCL height regimes. Lower LCLs during low stratiform periods are consistent with cooler and moister
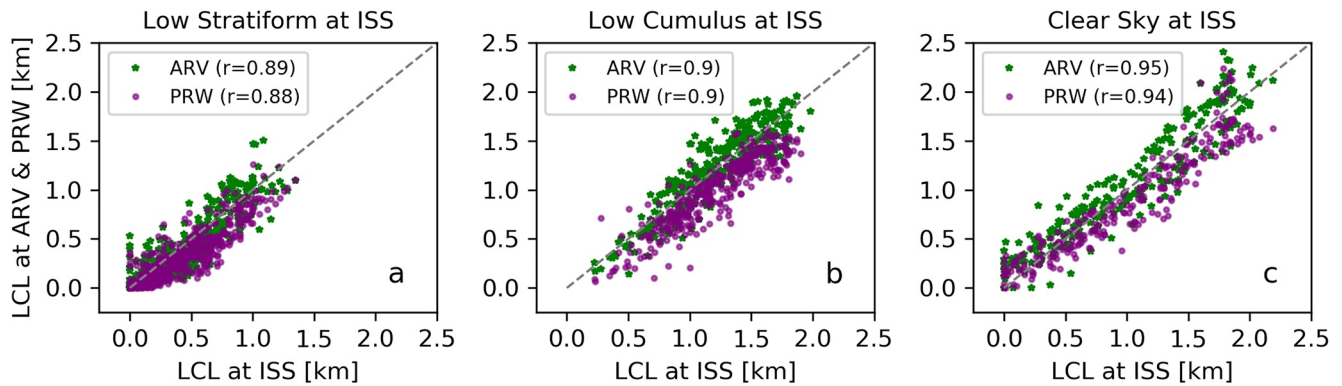
Figure 7. Spatial comparisons of lifting condensation level (LCL) [km] at ARV (green) and PRW (purple) compared to the LCL at integrating sounding suite (ISS). Panels separate the LCL comparison into the following periods of consecutive sky conditions at ISS: (a) low stratiform; (b) low cumulus; and (c) clear sky. Correlation coefficients (r) between the spatial comparison of LCLs in each panel's legend).

conditions during this cloud regime (Figure 4). The range of LCL heights (Figure 7c) was largest for the clear sky regime. Clear sky periods were dominant during early morning, and the general diurnal cycle of the LCL, which starts relatively shallow in the early morning and rapidly grows (Haiden, 1997) is reflected in the wide range of observed clear sky LCLs.

A lack of scatter between LCLs at ARV and PRW for a particular cloud regime observed at ISS indicates thermodynamic conditions across the spatial domain of CHEESEHEAD19 were frequently quasi-constant. This supports the notion that large-scale forcing was similar across the approximately 50 km domain during a particular cloud regime. While the same sky condition did not always occur at the same time between the three sites (slight differences in Figures 2a–2c), the state of the lower atmosphere was generally consistent. However, the LCLs were systematically lower at PRW relative to those at both ISS and ARV. Investigation revealed that near-surface dew point depressions tended to be smaller at PRW, on average by approximately 2°C. Corresponding higher near-surface relative humidity at PRW caused a shift toward lower LCLs compared to the other two sites.

Differences in LCL clustering for different sky conditions further indicate a separation amongst cloud regimes. LCLs were clustered on the low range under low stratiform periods (Figure 7a), clustered higher during periods of low cumulus (Figure 7b), and across a wider range of heights during clear skies (Figure 7c). Because of the general LCL clustering and separability between sky conditions, an ensemble-style analysis to compare SEB and boundary layer structure responses to different cloud types is justified.

3.2. Surface Energy Budget

The SEB determines the net energy transfer at the land-atmosphere interface, and is defined as the following balance in energy between the atmosphere and the land surface:

$$R_{net} = G + H_s + H_l + S \tag{1}$$

where the net radiative fluxes (R_{net} = SWD-SWU + LWD-LWU; LW = longwave, D = downwelling, U = upwelling) and the transfer of ground heat flux (G) to or from the interfacial surface determine the energy available to be partitioned into turbulent sensible (H_s) and latent (H_l) heat fluxes, and S represents the changes in the system enthalpy (heat or photosynthetic storage). During the daytime over land, the SEB is primarily driven by the solar diurnal cycle, and the presence or absence of clouds has a significant impact on SWD, and to a lesser extent the LWD, and subsequently the turbulent exchange processes. To understand how boundary layer clouds impact radiation and therefore influence the efficiency of turbulent heat exchange, scatterplots of $H_s + H_l$ versus R_{net}-G are examined (Figure 8).

The linear regression slope values shown represent the turbulent heat flux exchange of the net surface radiative energy, which is relatively efficient for all sky conditions (Figure 8a). Linear regressions for morning and afternoon periods split into equal solar elevations capture over 85% of the variance while indicating a turbulent exchange efficiency near 80%. An energy imbalance, or residual, of 20% is not uncommon with a 30 min averaging
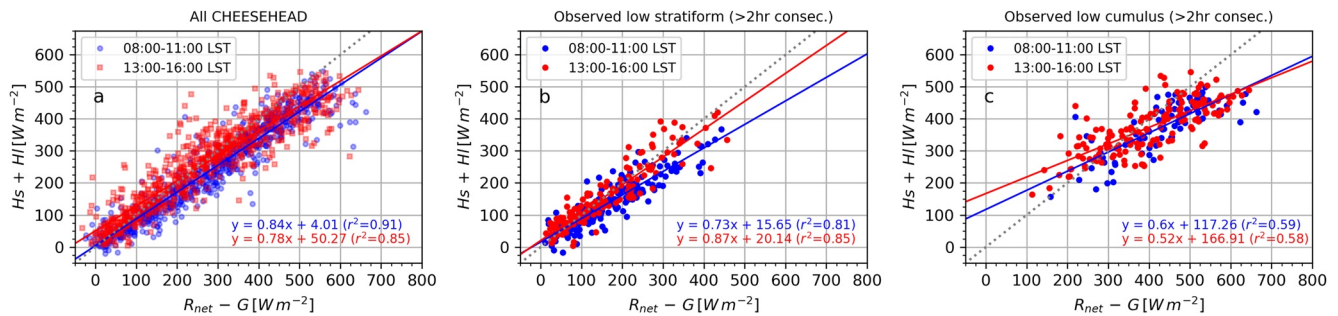
Figure 8. Scatter plot relationships between the turbulent heat fluxes ($H_s + H_l$ [W m^{-2}]) and net radiation (R_{net}) minus ground heat flux (g) for (a) all Chequamegon Heterogenous Ecosystem Energy-Balance Study Enabled by a High-Density Extensive Array of Detectors 2019 observations; (b) for consecutive low stratiform periods; and (c) consecutive low cumulus periods. Colors represent 3 hr periods observed during the morning (blue) and afternoon (red) in local standard time (LST). Linear regression equations and r^2 values were included for each morning/afternoon period. Black dotted line is the 1:1 relationship.

period (Grachev et al., 2020) considering the canopy energy storage term is not included nor is sampling uncertainty. Following the best-fit linear slopes, turbulent partitioning of R_{net}-G was approximately 6% more efficient in the morning compared to the afternoon. Shifting efficiency in turbulent exchange was also reported at field observations from the southeastern United States although exchange efficiency was always slightly greater in the afternoon compared to the morning (Lee et al., 2019).

Just as the different cloud types significantly impact SWD, the THFs respond accordingly to the availability of surface energy. THFs under low stratiform clouds only intermittently exceeded 300 W m^{-2} regardless of time of day while they rarely dropped below 200 W m^{-2} under low cumulus skies (Figures 8b and 8c). Linear fits of the response of THFs during low stratiform periods ($r^2 > 0.81$) in comparison to low cumulus ($r^2 \sim 0.6$) reveal a substantial decrease in exchange efficiency for cumulus cloud conditions. In addition, large, positive regression offsets (117–167 W m^{-2}) indicate a larger influence of hysteresis between the radiative energy input and production of turbulent exchange under low cumulus compared to periods of low stratiform (15–20 W m^{-2}). Under low stratiform clouds, THF exchange efficiency is larger by nearly 15% during the afternoon compared with the morning, unlike the diurnal partitioning seen in Figures 8a and 8c where the morning exchange exceeded the afternoon. For comparison, THF exchange efficiency during consecutive periods of clear skies yielded a slope of 0.95 (not shown), suggesting very efficient partitioning of radiative to turbulent energy under cloud free skies. Sky conditions overhead, therefore, exert substantial control on the daytime SEB with a potential forcing back onto the cloud evolution.

The inability to close the SEB, resulting in a residual flux of available energy, is common amongst finite measurement systems (Butterworth et al., 2021; Grachev et al., 2020). Examples of the surface energy residuals (SEB$_{res}$) under the different cloud conditions are shown in Figure 9. The SEB$_{res}$ are plotted against the surface net radiation minus the ground heat flux (R_{net}-G) for the cloud types in Figure 9a, while the RFDs of the SEB$_{res}$ are shown in Figure 9b. The scatter plot reveals that under low stratiform and low cumulus clouds, the SEB$_{res}$ typically increase as R_{net}-G increases, although the relationship may not be linear. This is expected since the THFs will increase in response to the larger radiative forcing at the surface but with a certain degree of lag, or hysteresis. The larger scatter in the SEB$_{res}$ found during low cumulus periods suggests the hysteresis of THF response to R_{net} is enhanced for these cloud periods compared with low stratiform periods.

Under clear sky conditions, the SEB$_{res}$ distribution mainly ranged between 0 and 100 W m^{-2} (Figure 9b). Differences in the distributions between the BL cloud periods and clear sky periods reveals how the clouds modulate the surface radiative fluxes and how this impacts the response of the THFs. Under low stratiform cloud periods that frequently occurred during early morning (as well as more frequently during autumn than summer, Figures 2 and 3), R_{net}-G remains relatively small. The limited incoming energy delays the change in sign (or direction) of the THFs from negative (atmosphere to the surface) to positive (surface to atmosphere). Low cumulus periods also had a considerable number of SEB$_{res}$ below 0 W m^{-2}, however, these are not associated with near-surface static stability (as will be discussed later). Instead, the broken cloudiness that is characteristic of low cumulus clouds causes a decrease in the R_{net} due to the shading of direct beam solar radiation. The THFs, however, do not respond as rapidly to the changing radiative forcing because of the thermal inertia of the ground and canopy
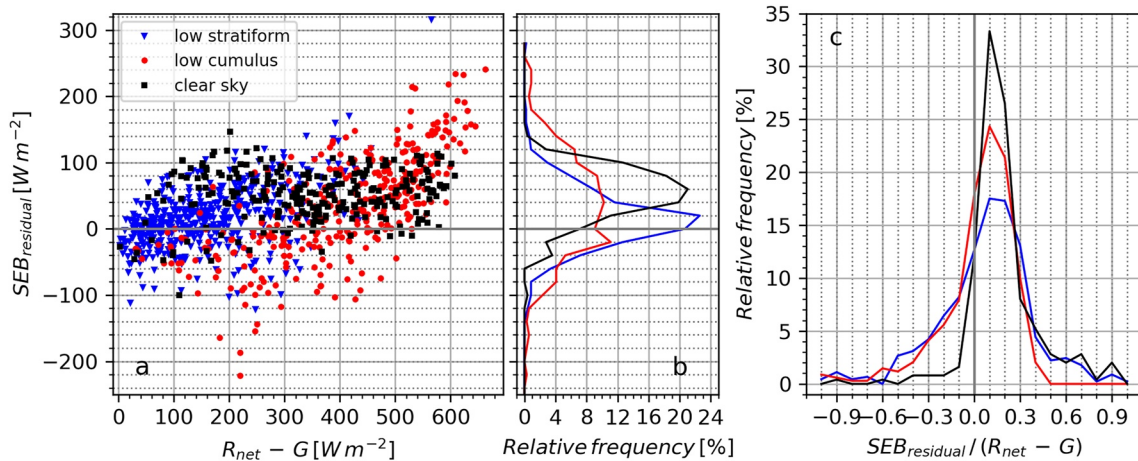
Figure 9. (a) Scatter plots of the residual surface energy budget (SEB) (SEB_res [W m^{-2}]) against R_{net}-G [W m^{-2}] per cloud type; (b) relative frequency distributions [%] of the SEB_res per cloud type (corresponding to y-axis of panel a); and (c) relative frequency distributions [%] of SEB_res weighted by the available radiative energy at the surface (R_{net}-G) per cloud type.

and thus remain large and directed from the surface to the atmosphere (net loss), resulting in relatively frequent negative SEB$_{res}$ (Figure 9b).

The magnitudes of the SEB$_{res}$ were dependent upon the cloud type (Figure 9b); it is expected that the residual energy should contribute to the local storage of heat within the canopy and warming of the surface during periods of clear sky and low cumulus, or lack thereof for low stratiform, potentially contributing to the development of buoyant circulations sustaining the cumulus cloud fields. However, regardless of cloud type, when weighting the SEB$_{res}$ by the incoming radiative energy (R_{net}-G) the distributions were comparable amongst these periods (Figure 9c). The residual energy primarily corresponds to a range of −10% to +30% of the net surface radiation, a range reported as typical for energy balance studies from a discrete set of SEB station measurements (Butterworth et al., 2021). Positive tails of the distributions were limited to about 0.3 under low cumulus but were considerably longer, albeit more infrequent, for low stratiform and clear sky periods. Long, positive distribution tails are a result of the frequent early morning start times of these consecutive periods; the lower solar elevations (high solar zenith angles) during the morning limit SWD (Figure 2d). Oppositely, residuals rarely fell below −0.1 for clear sky conditions, while longer, negative tails exist for both boundary layer cloud types.

3.3. Cloud Radiative Forcing and THF

Shortwave cloud radiative forcing (CRF$_{SW}$) is a measure that quantifies the impact clouds have on solar radiation, defined as the difference between all-sky and clear-sky SWN:

$$CRF_{SW} = (SWD_{all\text{-}sky} - SWU_{all\text{-}sky}) - (SWD_{clear\text{-}sky} - SWU_{clear\text{-}sky}) \qquad (2)$$

Clear sky radiative fluxes are estimated using the Radiative Flux processing analysis (Long & Ackerman, 2000). As clouds typically attenuate shortwave radiation, CRF$_{SW}$ at the surface is negative, resulting in a relative cloud cooling effect (e.g., Ramanathan et al., 1989). The CRF$_{SW}$ observed for the two low cloud types shows a wide range, from quite strong, −600 W m^{-2}, to quite modest near 0 W m^{-2} (Figure 10a). Subsequently, THFs respond to the modification of SWD by the cloud type. Under low stratiform periods, individual scatter points of H$_s$ + H$_l$ were frequently observed between 0 and 300 W m^{-2} and correspond to a median CRF$_{SW}$ (black square within blue scatter) approximately −300 W m^{-2}. The relatively large reduction in solar radiation causes a THF-limited regime such that the upper quartile range of THFs (blue shading) rarely exceeds 200 W m^{-2}. Under low cumulus, the THFs were significantly larger, often 300–500 W m^{-2}, in line with a weaker CRF$_{SW}$ whose median value was only −50 W m^{-2} (black square within red scatter). Longer periods of unattenuated, direct SWD between the broken low cumulus cloud fields supported larger THFs. Additional SWD as a result of the positive cloud effect (enhanced diffuse scattering combined with unattenuated direct irradiance in broken cloud fields leading to greater than clear sky SWD) causes some instances of CRF$_{SW}$ > 0 W m^{-2}. Median THFs for clear sky conditions
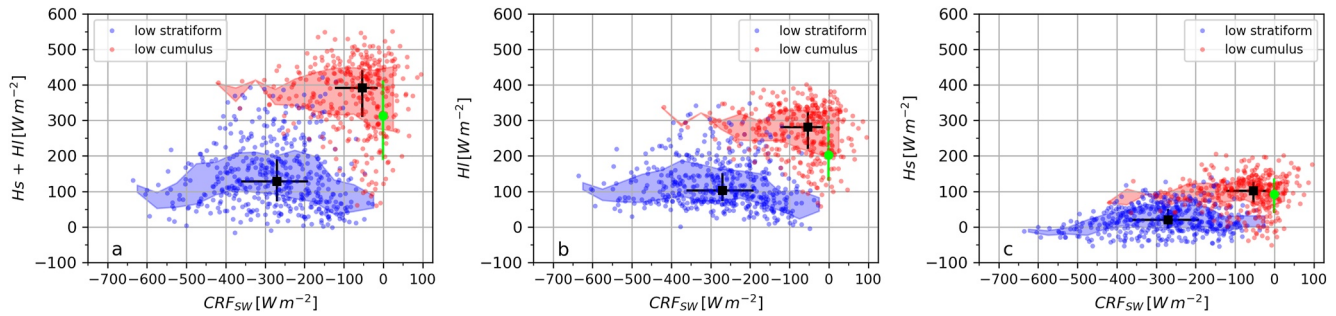
Figure 10. Scatter plot relationships between (a) $H_s + H_l$ and shortwave cloud radiating forcing (CRF_{SW}); (b) H_l and CRF_{SW}; and (c) H_s and CRF_{SW}, for low stratiform (blue) and low cumulus (red) periods, all in W m^{-2}. Shading represents the 25th-75th interquartile range in H_s and H_l per 50 W m^{-2} CRF_{SW} bins. Black squares and lines represent the median values and interquartile ranges for CRF_{SW}, H_s, and H_l per cloud type; the green circles and lines are the medians/interquartile ranges for clear sky periods.

(green circle) were approximately 100 W m^{-2} less than those under low cumulus; CRF_{SW} under clear sky conditions is by definition 0 W m^{-2} (Equation 2). When comparing the median THF values, a factor of three increase was observed for low cumulus periods compared to low stratiform. Such increases in L-A energy exchange support the low cumulus lifecycle by providing the heat and moisture to the upper portion of the boundary layer through convection.

Separating THFs into H_l (Figure 10b) and H_s (Figure 10c), it is clear the daytime cloudy surface fluxes at CHEESEHEAD19 were dominated by H_l. Contrast this with results from a Canadian mid-latitude lichen woodland station and the ARM Southern Great Plains (SGP; Sisterson et al. [2016]) central facility in north-central Oklahoma, where THFs measured when warm-season low cumulus were observed were controlled by H_s, which ranged from approximately as large, to nearly twice as large, as H_l (Fitzjarrald & Moore, 1994; Lareau et al., 2018; Zhang et al., 2017). At CHEESEHEAD19, latent fluxes were always positive regardless of cloud type, while sensible flux could be negative, resulting in heat transfer from the atmosphere down to the surface. While $H_s < 0$ W m^{-2} were more frequent during low stratiform periods, some negative values were observed with low cumulus for relatively small CRF_{SW} (>−100 W m^{-2}). Values of H_s during low cumulus days at ARM SGP and in Canada ranged 200–300 W m^{-2} during peak summer (Fitzjarrald & Moore, 1994; Tao et al., 2019), considerably larger than the 100–150 W m^{-2} range at CHEESEHEAD19.

Despite some outlying scattered values, the median and interquartile ranges of H_l and H_s both differed by a factor of three between the two cloud scenes; median H_l and H_s varied only by a factor of two when skies were clear. At the SGP site, multiple years of H_l and H_s measurements differed only by a factor of two or less during summer all-sky conditions (Tao et al., 2019), similar to the clear sky median values in Figures 10b and 10c. The different THF responses per a particular cloud type at CHEESEHEAD19 suggest the different surface characteristics play an important role in SEB evolution. Reduction in solar shading during periods of broken cumulus supports more THF exchange at the surface, likely contributing to feedback supporting cloud lifecycle through turbulence production and buoyant circulations. Clear sky THFs were slightly smaller than those during low cumulus. Further discussion on the implications of enhanced THFs during cumulus periods is given below.

3.4. Soil Moisture and Surface Fluxes

To determine whether soil moisture variability supported different sky conditions during CHEESEHEAD19, the relationships between H_l and Evaporative Fraction (EF = $H_l/(H_l + H_s)$) with volumetric soil moisture were explored (Figures 11a and 11b). While the range of Hl was large, soil moisture was mainly confined in a range between 23% and 33% for all sky conditions. Because the range in H_l for given soil moisture was wide, no systematic link between larger volumes of soil moisture contributing to larger H_l was observed. Values of EF for low cumulus and clear sky periods were tightly clustered between roughly 0.6 and 0.8 and also did not vary much with soil moisture. A lack of variability in EF also supports the notion that sufficient near-surface moisture is present during low cumulus as well as clear sky periods, and the level of moisture in the soil does not necessarily dictate the magnitude of H_l. These sky conditions, therefore, do not identify with a regime that is limited by the presence of moisture near the surface (Gentine et al., 2007, 2011). At soil moisture volumes above 33%, a handful
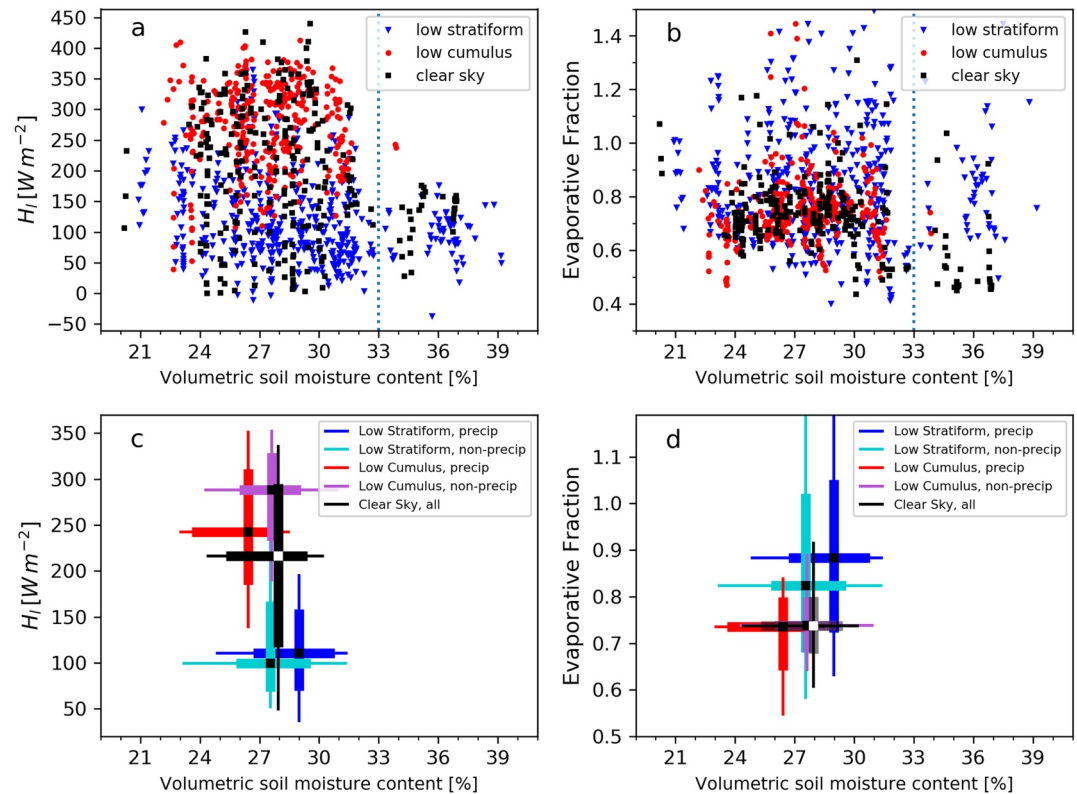
Figure 11. (a) H_l [W m^{-2}] vs. volumetric soil moisture content [%] and (b) evaporative Fraction (EF) [W m^{-2}] versus volumetric soil moisture content for consecutive sky condition periods: low stratiform (blue triangles), low cumulus (red circles), and clear skies (black squares). 10th-90th (lines), 25th-75th (bars), and medians (squares) distributions of the relationships between (c) H_l and (d) EF against volumetric soil moisture content. Different colors represent distributions for different cloud regimes and whether or not precipitation was observed within a 6 hr window prior to each cloud regime.

of cases of clear sky periods had EFs systematically lower than 0.6–0.8; further investigation revealed a link to the seasonal evolution and a decrease of H_l (see Figures 11a) relative to H_s (not shown). With low stratiform clouds, EF had the greatest variability, although, as observed with the other two sky conditions, no clear partitioning with volumetric soil moisture was determined.

The large, but the relatively similar scattered relationship between H_l and EF for a given volume of soil moisture suggests that soil moisture was not the emergent forcing on local cloud type. The influence of rain events on the soil moisture and surface flux partitioning relationships are shown statistically in Figures 11c and 11d. Shown are the interquartile and median distributions (bars and squares, respectively) during the different sky condition periods but separated by whether or not a rainfall event was observed during a 6 hr period prior to the onset of the sky condition period. Periods of rainfall were determined by examining 10 min mean attenuated backscatter profiles from the ceilometer at ISS for attenuation that extended from a level in the atmosphere and remained continuously attenuated to the lowest 10s of meters above the surface. The 6 hr window prior to the low cloud or clear sky regime were identified to be under the influence of rain if at least 20% of the 10 min observations within that 6 hr window (over 1 hr total) were flagged as precipitating (blue and red ranges), or non-precipitating if less than 20% of the profiles did not identify as rain (teal and purple ranges). Statistical relationships are shown in Figures 11c and 11d were only computed for volumetric soil moisture contents <33% to avoid contamination by the limited observations with soil moisture above that level (dashed vertical line in Figures 11a and 11b).

The frequency of rainfall events prior to a particular sky condition differed widely. Rain occurred most frequently before low stratiform periods, 22 times out of a total of 48 periods (46%), dropping in frequency to only 8 of 46 low cumulus periods (17%). Only 3 clear sky periods from a total of 22 (14%) had rainfall during the prior 6 hr period; therefore, clear sky periods were treated altogether with no attempt to distinguish the three precipitating cases. The lack of a large number of precipitating events preceding low cumulus cloud periods implies the larger
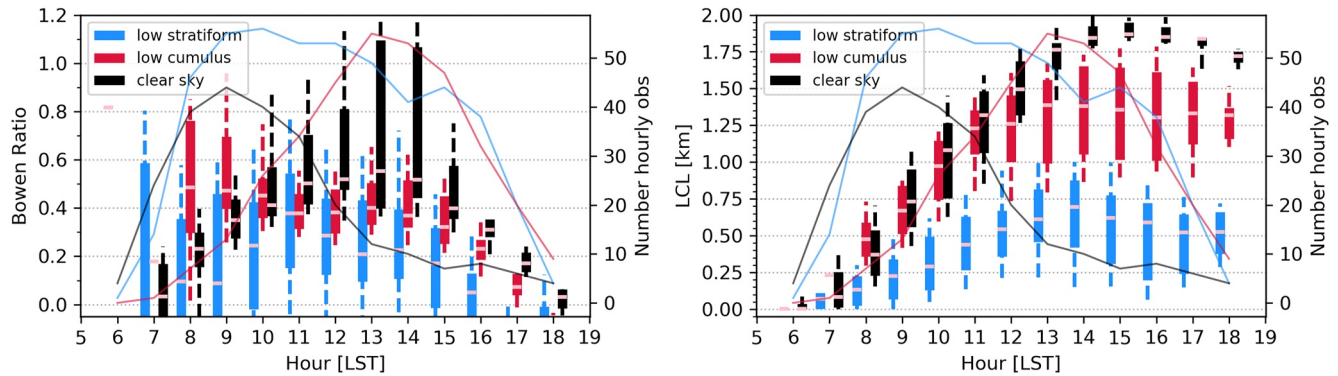
Figure 12. Statistical distributions of the diurnal evolution of (a) Bowen ratio and (b) lifting condensation level [km] by cloud regime (colors). Pink lines are the hourly medians, thick bars the 25th-75th interquartile range, and the dashed lines the 10th-90th range. Number of data points populating the statistics for each hour are represented in the thin colored lines (corresponding to *y*-axis on righthand side).

fluxes of H_l are not contingent upon rainfall to precondition the cloudy mixed layer. Soil moisture medians and interquartile ranges during low cumulus periods were also larger when the window prior to cumulus was non-precipitating. Likewise, ranges of H_l during non-precipitating periods prior to low cumulus were also larger than prior precipitating periods. However, the range in EF did not vary with rainfall events, which indicates changes to H_l are correlated with changes to Hs. And while the spread in H_l for clear sky periods was smaller than low cumulus, the range in soil moisture, even when precipitation was observed prior to low cumulus, was larger during clear periods. Precipitation prior to low stratiform clouds did lead to an increase in soil moisture, as well as modest increases in H_l and EF, relative to non-precipitating periods prior to the cloud onset.

A tight coupling between the diurnal evolution of near-surface turbulent heat fluxes and LCL level was found for all sky conditions (Figure 12). Ample moisture near the surface causes the Bowen ratios ($B = H_s/H_l$) to increase slowly during low stratiform periods, constrained well below 0.5. Corresponding LCLs were limited in their growth rates (Haiden, 1997) during morning hours and remain starkly lower than clear sky and low cumulus cloud regimes. Meanwhile, for the clear sky and cumulus regimes, mid-morning B and LCL growth were similar and exceed those observed with low stratiform clouds. By late morning, a separation between low cumulus and clear sky B occurred. With low cumulus, median B asymptote near 0.4 and LCL heights remain lower than the continually deepening LCLs of clear sky conditions: note the number of clear sky periods drops dramatically after 12:00 LST and the statistics are therefore skewed toward only a handful of observations. Enhanced H_l relative to H_s exerts an important control on limiting the growth of the LCL height (Haiden, 1997), ultimately supporting the formation of cumulus cloud fields as daytime convection continues to evolve. Considering the similar H_s between low cumulus and clear sky regimes (Figure 10c), increased surface evaporation and evapotranspiration support an increased H_l which preconditions the late morning mixed layer for low cumulus onset; the lack of systematic response of soil moisture to rainfall prior to low cumulus or clear sky regimes suggests the extent of near-surface evaporation from dew or rain on vegetation during the early morning is an important mechanism in supporting or inhibiting cumulus formation (Lareau et al., 2018).

3.5. Turbulent Scale Statistics

Surface layer turbulent heat fluxes are modulated by the relationships between scalar gradients (temperature and humidity) and near-surface winds. The surface shear stress can be written as the square of a velocity scale known as the friction velocity (u_*) based on the longitudinal and latitudinal momentum stresses

$$u_* = \left[\overline{u'w'}^2 + \overline{v'w'}^2 \right]^{1/4} \tag{3}$$

The magnitude of surface turbulence, therefore, varies with gradients in horizontal wind speed, and also with the roughness elements of the surface and atmospheric stability. A relationship between mechanically-sustained turbulence and buoyancy-driven turbulence is made through the Obukhov length scale (L)
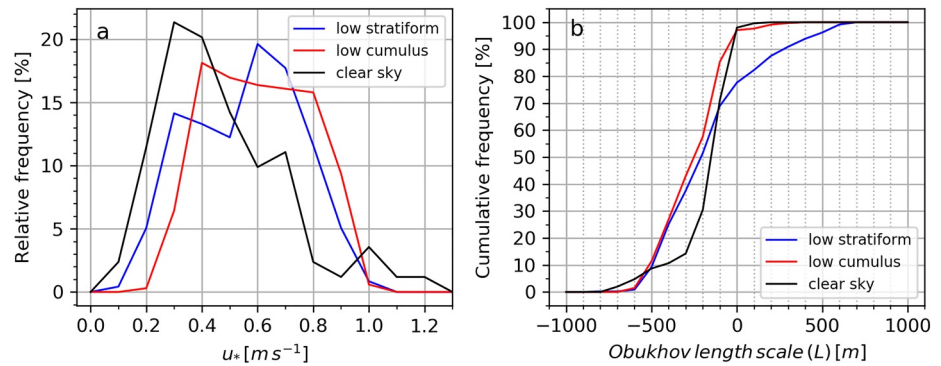
Figure 13. (a) Relative frequency distributions [%] of u_* [m s^{-1}] and (b) cumulative frequency distributions of Obukhov length scale (L, [m]) for observed during consecutive cloud type periods: low stratiform (blue); low cumulus (red); and clear sky (black).

$$L = \frac{-\overline{T_v}u_*^3}{kg\overline{w'T_v'}} \tag{4}$$

where $\overline{T_v}$ is the mean virtual temperature, k the von Karman constant (0.4), and $\overline{w'T_v'}$ the kinematic heat flux. The sign of L is characteristic of the static stability while the magnitude is characteristic of the height where buoyant production of turbulence equals that of shear production. Typically, L is used in relating to a physical height within Monin-Obukhov similarity theory to non-dimensionalize surface layer turbulence (e.g., Stull, 1988).

Statistical distributions of u_* and L for the low cloud types and clear skies reveal unique behaviors associated with different sky conditions. The friction velocity RFD under clear sky has a well-defined distribution peak at relatively small $u_* = 0.3$ m s^{-1} (Figure 13a, black). Analogously, Obukhov lengths were exclusively negative and most often with L between -250 m and 0 (Figure 13b). These results reveal the surface layer during clear sky conditions at CHEESEHEAD19 was statically unstable and turbulence was driven primarily by buoyancy circulations forming close to the surface.

During conditions of low, boundary layer clouds, u_* was considerably larger than when skies were clear. Distributions of u_* for both low cumulus and low stratiform periods indicate a local distribution peak at small friction velocities (0.3–0.4 m s^{-1}) similar to the peak observed for clear skies. The difference, however, is the lower u_* values represented the primary distribution mode for low cumulus although the peak is relatively flat and does indicate occasionally large (>0.8 m s^{-1}) velocities. The peak mode during low stratiform clouds was larger, near 0.6 m s^{-1}. Shear production of turbulence was therefore substantial under the overcast, low stratiform cloud periods and seemed to vary more between relatively small and relatively large values under the broken, low cumulus cloud fields. The increase in u_* for low stratiform periods could also be associated with a change in the surface roughness elements and the primary wind fetch. Distributions of wind direction did indicate differences in air mass origin between low stratiform and low cumulus (Figure 4f), even though wind speeds were similar between the cloud regimes (Figure 4e).

In terms of static stability within the surface layer, Obukhov length scales during clear sky periods were different from the BL cloud periods. Length scales were typically smaller than -200 m, a range that represents static instability and is conducive to convective mixing (Krishnamurthy et al., 2021). A similar distribution of Obukhov lengths was reported for clear sky conditions at SGP (Berg et al., 2017). For Obukhov length scales below -300 m, the distributions under low stratiform and low cumulus cloud periods were nearly identical (Figure 13b). These values of L typically are found under near-neutral instability (Krishnamurthy et al., 2021) where shear production of turbulence dominates over buoyant production across a deeper layer. Smaller but negative L (between -200 m and 0) were observed more often under low cumulus clouds than low stratiform; about 40% compared to 23% of all Obukhov lengths for low cumulus and low stratiform, respectively, were observed in this unstable regime where buoyant turbulent production matched shear production across a relatively thin layer. The cumulative frequency increase for this range of L was similar to the clear sky periods, suggesting the relatively unattenuated solar radiation at the surface was responsible for producing the thermally-driven buoyant heat
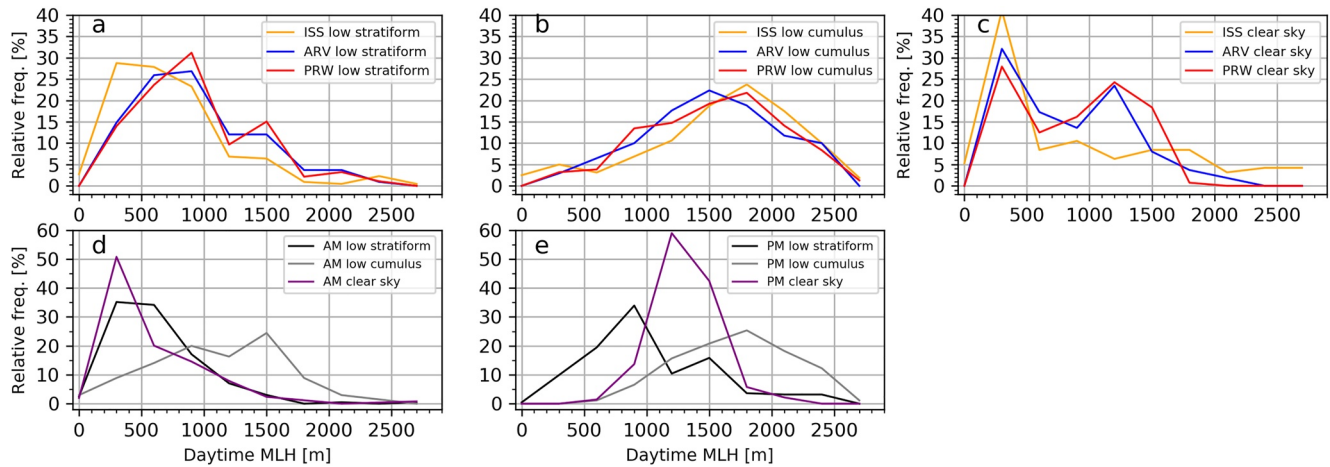
Figure 14. (a)-(c) Relative frequency distributions [%] of daytime mixed layer height [MLH, m] for (a) low stratiform periods, (b) low cumulus periods, and (c) clear sky periods. Distributions are shown for the three observational locations: ISS (yellow), Lakeland (ARV) Airport (blue), and Prentice (PRW) Airport (red). (d) Relative frequency distributions of mixed layer height for morning (AM) periods and afternoon (PM) periods, computed by combining mixed layer heights from the similar cloud types at all three locations: low stratiform (black), low cumulus (gray), and clear sky (purple). MLHs are retrieved from the RWP at ARV and PRW and from the ceilometer at ISS.

fluxes. Oppositely, a substantial fraction, more than 20%, of low stratiform periods were associated with positive L. For these periods, static stability prohibits buoyant turbulent production, and instead the turbulent heat fluxes are dependent upon mechanical production through horizontal wind shear.

3.6. Mixed Layer Height Response to Cloud Regime

Differences found in the SEB, THF exchange partitioning, and turbulence production scales for different sky conditions are likely to force a response or feedback in the growth of the daytime mixed layer height (MLH; also referred to as daytime boundary layer height). The distributions of MLH depth (Figures 14a–14c) per cloud type reveal unique differences associated with a particular cloud type while the distribution shapes were broadly similar amongst the three locations. The depth of the mixed layers was largest under low cumulus clouds where peak MLH distributions ranged from 1,500 m to 1,800 m above ground level (AGL; Figure 14b). Oppositely, the smallest MLH depths ranging between approximately 500-1,000 m AGL occurred during low stratiform periods. The distributions of MLHs were also relatively shallow under clear sky conditions (Figure 14c) however for the ARV and PRW airports these clear sky distributions were bi-modal with secondary peaks around 1,200 m AGL. At ISS, the distribution shapes under low stratiform and clear sky conditions were slightly different compared to the airports. At the airports, MLH was retrieved from the 915 MHz radar wind profiler, while at the ISS the heights were retrieved from profiles of ceilometer attenuated backscatter. Differences in the measurement principles and subsequently in the retrieval algorithms contributed to the spatial differences seen in MLH distributions (Duncan et al., 2021).

Deeper MLHs under low cumulus clouds compared to low stratiform clouds suggest a response where larger surface solar heating and turbulent heat flux redistributions contribute to the vertical growth of the mixed layer. While the clear sky MLH distributions indicate a mode of deeper MLHs around 1,200 m AGL, these modes were still considerably shallower than the 1,500–2,000 m AGL peaks for low cumulus.

The shallower MLH development under clear sky conditions may be linked to feedback associated with increased entrainment associated with the low cumulus cloud fields. Figure 14 d-e suggests the MLH may also be determined by the diurnal preference of different BL cloud types observed during CHEESEHEAD19. During the morning (AM: prior to 12:00 LST), MLHs were, in general, lower than during the afternoon (PM: after 12:00 LST) for all three sky conditions. MLHs were predominantly below 600 m AGL during the morning period under clear sky or low stratiform conditions; the peak MLH was even below 400 m AGL during clear sky conditions. Generally, as both low stratiform and clear sky consecutive 2 hr periods commenced during the early-to-mid morning hours (Figure 2d), the associated lower MLHs dominated the distributions at the different sites
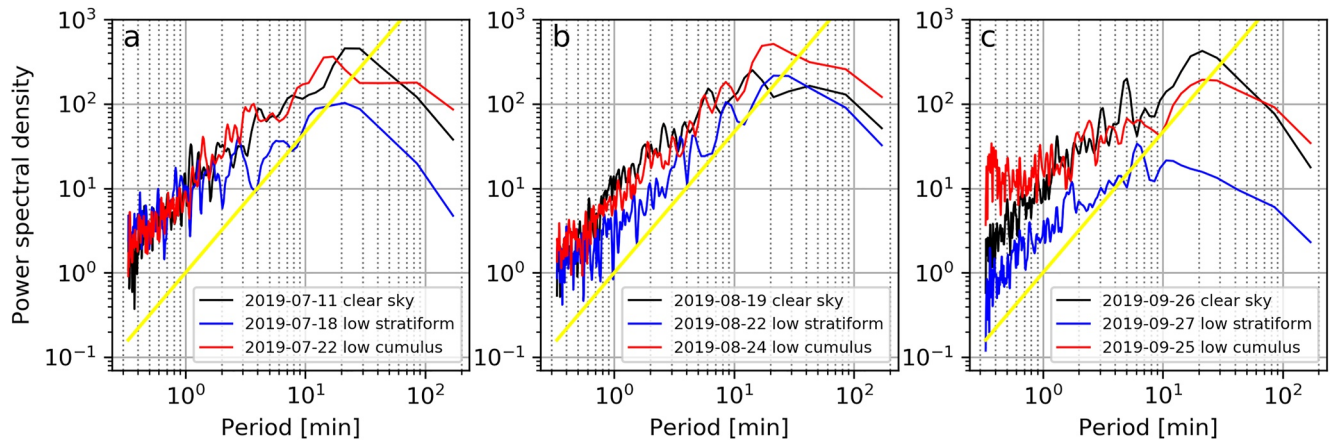
Figure 15. Power spectral densities of daytime vertical velocity (w, [m s^{-1}]) from the Doppler lidar. Observations of w are from the middle of the mixed layer ($z/z_i = 0.5$) for 3 days that were predominantly clear skies (black), low stratiform (blue) or low cumulus (red) for during the month of (a) July; (b) August; and (c) September. The −5/3 slope line is shown in yellow.

(Figures 14a and 14c). MLHs ranging from 1,000 to 1,500 m AGL were observed when low cumulus was present during the morning.

By the afternoon, MLHs grew in depth for all three sky conditions (Figure 14e). The afternoon clear sky MLH distribution revealed the largest relative growth in MLH compared to the morning distributions. However, only 30 clear sky afternoon events of at least 2-hr duration were observed compared to 139 > 2-hr morning events. MLHs under low stratiform clouds were generally limited in their growth potential, unlike under low cumulus where the majority of MLHs were substantially greater than 1,000 m AGL. When comparing low stratiform and low cumulus MLHs, increased SWD leading to increases in surface THFs associated with the latter cloud type contribute to the daytime convective mixing and overall boundary layer deepening. This is consistent with an increased occurrence of Obukhov lengths scales representing statically unstable conditions under low cumulus, suggesting increased turbulent mixing through buoyancy. Intriguingly, median H_s was only about 100 W m^{-2} during low cumulus, while H_l was nearly three times as large. The transfer of ample radiative heat to latent heat as an important source of moisture to the broken cumulus cloud fields is apparent, consistent with higher temperatures and lower near-surface relative humidity (Figures 4a and 4b) supporting the latent heating process. This surface source of moisture is important in sustaining low cumulus as rising air parcels are lifted to higher MLHs, with the parcels ultimately subjected to stronger adiabatic cooling.

3.7. Variability in Vertical Velocity With Sky Condition

Using 1-hr averages of MLHs to normalize the depth of the layer, power spectra of lidar-measured vertical velocity (w) as a function of frequency are compared for three days each month (a: July; b: August; c: September) of CHEESEHEAD19 predominantly influenced by the three sky conditions (Figure 15); sky condition days each month were chosen within approximately 10 days to ensure similar solar forcing. The power spectra were calculated from time series of w at $z/z_i = 0.5$ for each day, where z_i is the daytime 1-hr mean MLH.

A prototypical decay in w spectral density occurs for all months and cloud types as the period decreases. Generally, the power spectra reveal a decay in variance on a rate that mimics a slope of −5/3 (yellow lines) starting around periods between 3 and 10 min. As such, the energy associated with perturbations in w indicates the energy cascade transfer from larger eddies to smaller perturbations where dissipation is ongoing (Stull, 1988). The largest spectral peaks occurred at periods ranging between approximately 15 and 25 min, the exception being the low stratiform day during September when the peak variance period was observed near 6 min (Figure 15c). Variance in w produced on these longer periods is likely associated with larger-scale forcing and is not associated with the turbulent kinetic energy produced through surface turbulent eddies.

From Figure 15, it is evident the w variance in the middle of the mixed layer is similar between the clear sky and low cumulus days. The total variance in w tended to be slightly larger for the low cumulus days than for the
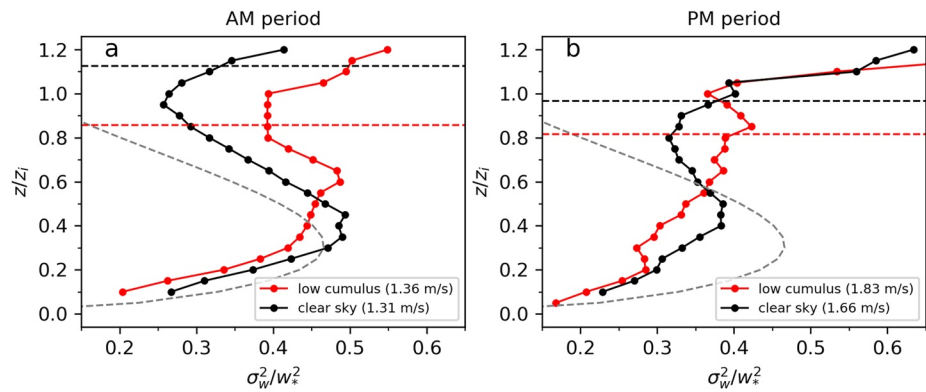
Figure 16. Normalized (z/z_i) profiles of mean vertical velocity variance (σ_w^2) weighted by the mean convective velocity scale (w_*) for low cumulus (red) and clear sky (black) days are analyzed in Figure 15. Panel (a) shows the mean profiles during the morning (AM period) and (b) during the afternoon (PM period). Dashed horizontal lines indicate the lowest normalized height where cloud base was observed for the 3 days; the vertical velocity profiles above this level should not be considered due to cloud attenuation of the Doppler lidar causing spurious vertical velocity estimates. The gray dashed line is the non-dimensionalized parameterization of σ_w^2 from Lenschow et al. (1980). Mean w_* used for scaling the AM/PM σ_w^2 are provided in the legends.

clear sky days. Total variance for the low cumulus and clear sky days were larger in September than July, with August actually having the smallest total variances of all the months. The same result was not observed for low stratiform days as the largest total variance occurred in July and decreased continually for the days during the subsequent 2 months; vertical motions experienced a substantive decrease in intensity as the season progressed. Total variance was always smallest during low stratiform days compared to the other sky conditions, a result that is consistent with the shallower mixed layer depths observed during low stratiform periods. As expected based on the THFs (Figure 10) and more frequent static instability within the surface layer (Figure 13b), low cumulus and clear sky conditions were characterized by enhanced turbulent mixing and buoyant overturning.

Figure 16 shows the morning and afternoon mean z/z_i profiles of vertical velocity variance (σ_w), computed as the average from the three low cumulus and three clear sky days examined in Figure 12. Velocity variance is scaled by the convective velocity scale w_*, which is defined as:

$$w_* = \frac{g z_i}{T_v}\left(\overline{w'T_v'}\right) = \left(\frac{-u_*^3 z_i}{kL}\right)^{\frac{1}{3}} \tag{5}$$

Scaling by w_* is traditional in Monin Obukhov similarity theory for a convectively-driven surface layer (e.g., Stull, 1988).

The non-dimensionalized profile parameterization of σ_w for the convective boundary layer proposed by Lenschow et al. (1980) (dashed gray) is shown for comparison. Also highlighted as horizontal dashed lines are the lowest normalized height (relative to z_i) where cloud base was encountered; note this level only demarks the lowest z_i where cloud base was observed for the 3 days and not all variance profiles encountered cloud level above this height. Profiles of σ_w^2/w_*^2 above these heights can include enhanced variance due to jumpiness in the retrieval of doppler velocity within cloudy volumes and should not be considered. Mean profiles of σ_w^2/w_*^2 for both sky conditions during the morning replicate the canonical increasing variance with height across the mixed layer (Lenschow et al., 1980). The transition where variance starts decreasing with height for mean clear sky profiles broadly matches with the parameterization and clear sky convective boundary layer behavior (Berg et al., 2017; Chandra et al., 2010; Zhou et al., 2019), while the profile for low cumulus days begins to decrease higher up, closer to the upper third of the mixed layer (Figure 16a). Similarly, for the afternoon, the clear sky profile decreases near the mid-point of the mixed layer (Figure 16b). Morning and afternoon profiles for both sky conditions are in broad agreement in σ_w^2/w_*^2 magnitude at scaled heights $z/z_i < 0.5$, even as the mean w_* (provided in the legend) was systematically larger under low cumulus.

Larger mean w_* for low cumulus limits the increasing shape of the profile below $z/z_i = 0.5$ relative to clear skies, especially in the afternoon. However, the enhanced variance between the middle of the mixed layer and
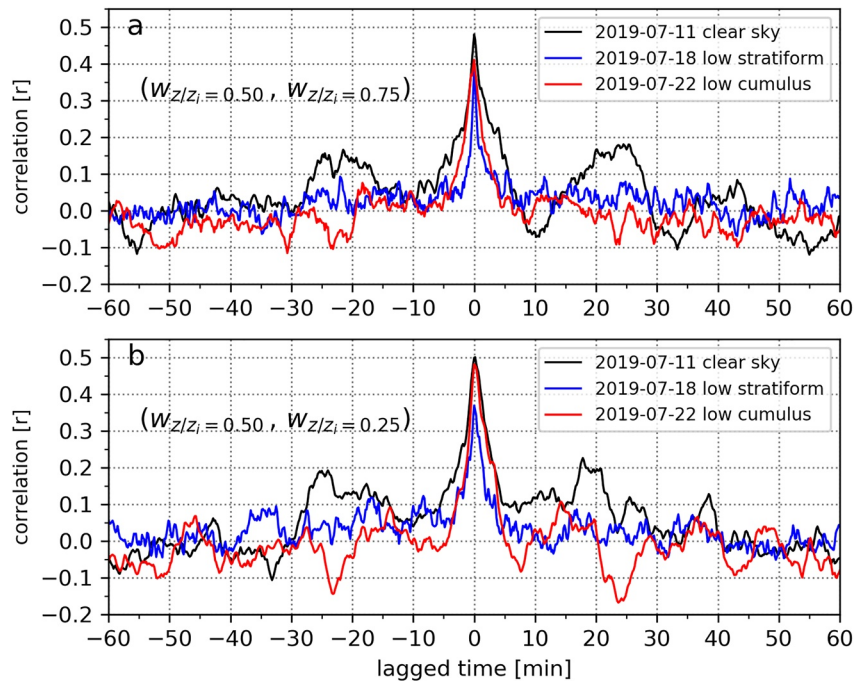
Figure 17. Time lagged [min] linear correlations (r) between vertical velocities at two normalized levels: (a) $z/z_i = 0.5$ and $z/z_i = 0.75$, and (b) $z/z_i = 0.5$ and $z/z_i = 0.25$. Observed correlations are computed for the same three sky conditions during July as in Figure 15a.

up to cloud base (dashed red line) is systematically larger when low cumulus was present. Interestingly, σ_w^2/w_*^2 profile statistics under shallow cumulus and clear sky conditions for multiple years at ARM SGP both revealed the canonical decrease above $z/z_i \sim 0.4$ (Lareau et al., 2018) in contrast to the present observations. Furthermore, Chandra et al. (2010) reported that velocity variance for clear sky days was slightly larger than for low cumulus days, a feature that is not observed during these days. The difference in mean profile shapes, namely continual increase with height under low cumulus relative to the decrease in σ_w^2/w_*^2 under clear skies suggests a difference in processes contributing to vertical velocity variance in the upper half of the mixed layer observed at CHEESEHEAD19. A potential explanation for the increased variance in vertical motion may be the enhancement of entrainment in the vicinity of low cumulus clouds and in the transition zones of clear air between cumulus clouds where subsidence may be enhanced. Exchanges of predominant updrafts to predominant downdrafts with low cumulus passage, in addition to potential lateral entrainment from saturated plumes, may contribute to the increased variance below cloud base height. Entraining drier air into the mixed layer may contribute to increasing the magnitude of H_l at the surface, and median H_l during low cumulus periods was on the order of 100 W m^{-2} larger than clear sky periods (Figure 10b). Normalized height profiles of w skewness from the distributions of vertical velocity were computed for these example days (not shown). During the afternoon above $z/z_i = 0.6$, mean skewness was systematically smaller during the low cumulus days relative to clear sky days although not statistically significant. The change in skewness matches the vertical levels where w variance was also systematically larger for low cumulus (Figure 16b). Smaller skewness is consistent with fewer occurrences of larger, upward vertical motions in the upper portion of the sub-cloud mixed layer, potentially signaling the emergence of more frequent downdrafts below the low cumulus cloud base. This shift in skewness between these sky conditions corroborates the potential for enhanced entrainment during the presence of low cumulus cloud fields. More cases are needed in order to further test this hypothesis.

To determine whether vertical motions displayed any degree of coherence across the mixed layer, lagged correlations were computed between $z/z_i = 0.5$ and $z/z_i = 0.75$ (upper quarter of mixed layer) and $z/z_i = 0.5$ and $z/z_i = 0.25$ (lower quarter). Figure 17 shows time-lagged correlations out to ± 60 min for the example sky conditions during July (see Figure 15a). During all three sky conditions, the maxima in vertical velocity correlations occurred near the zero lag and did not exceed 0.5, representing only 25% of the observed variance in correlating w between layers; maximum correlations were further reduced for the low stratiform day, reaching only $r = 0.35$ for the

lower quarter of the mixed layer (Figure 14b). With increasing time lag from zero, correlations fall relatively rapidly, especially for the low stratiform day when they drop well below $r = 0.1$ prior to reaching ±5 min lags. The low cumulus and clear sky correlations remain slightly higher at the 5 min lag indicating more vertical coherency compared to vertical motions across the mixed layer for low stratiform. The strongest correlations between time lags below approximately ±5 min are associated with coherent overturning circulations that span the general depth of the mixed layer. These timescales are also where the power spectra for w at $z/z_i = 0.5$ transition toward a slope of $-5/3$ (Figure 15).

Clear sky and low cumulus days also reveal a degree of periodicity present in w between the upper and lower quarters of the mixed layer. Correlations at the ±15–25 min lag are present for both layers under clear sky (black in Figures 17a and 17b). At similar time lags, an anti-correlation was observed under low cumulus and is more apparent for the correlation layer closer to the surface (red in Figure 14b). The 15–25 min time range was identified above as the peak frequency contributing to the w-variance at $z/z_i = 0.5$ (Figure 15). For these two sky conditions, a forcing is present at time scales that exceed those connected to the dominant mixed-layer scale eddies. An examination of visible satellite imagery from 22 July 2019 showed an organization of cumulus cloud streets (not shown) and suggests horizontal rolls may contribute to vertical motion coherency at longer lead times. Interestingly, for the low stratiform day, no apparent periodicity is found in w at the observed levels within the mixed layer. Cloud driven buoyancy forced by radiative cooling resulting in top-down convection represents the predominant forcing under the overcast stratiform cloud layer.

4. Summary

This study utilized the cloud regime classification model developed by Sedlar et al. (2021) to partition the daytime surface energy budget and boundary layer structure at CHEESEHEAD19 into three predominant cloud regimes: (a) low stratiform clouds, (b) low cumulus clouds, and (c) clear skies. We created ensembles consisting of periods greater than two consecutive hours for a particular sky regime to allow different forcings and responses of the surface energy fluxes to low boundary layer clouds over heterogeneous terrain to be analyzed and compared. As such, the regime separation has highlighted a number of key processes, including seasonal preference, contributing to the daytime mixed layer structure, which would have been difficult to disentangle without the cloud classification.

The occurrence of the different cloud regimes showed a distinct seasonality during the July-October 2019 period of CHEESEHEAD19. Both low cumulus and clear sky periods were most frequent during the "summer" months, followed by an increasing frequency of low stratiform periods from mid-August and onwards. As the seasons transitioned, the near-surface meteorological setting also varied. Warmer and drier months were associated with more cumulus or clear sky conditions, and the cooler, moister months had the more frequent overcast stratiform clouds. These seasonal transitions are consistent with observations of boundary layer cumulus from other midlatitude woodland studies (Fitzjarrald & Moore, 1994; Freedman et al., 2001). The conditions occurring under periods of low cumulus are broadly consistent with the prototypical low cumulus fields observed during the warm seasons observed at ARM SGP (Lareau et al., 2018) and midlatitude woodlands (Fitzjarrald & Moore, 1994; Freedman et al., 2001). These cloud fields are frequently thought to be controlled by the initial conditions of the surface properties and lower atmosphere thermodynamic structure early in the day (Findell and Eithar, 2003; Freedman et al., 2001; Rabin et al., 1990; Tao et al., 2019) and evolve with the diurnal cycle of the surface radiative and turbulent heat fluxes. Tight correlations between the LCL and cloud base height reveal the majority of these clouds were coupled with the surface, especially the cumulus clouds. The magnitude of shortwave radiation reaching the surface is strongly connected to the sky conditions overhead, as anticipated. The peak mode in downwelling shortwave radiation exceeded the peak mode for clear sky periods by approximately 25–100 W m^{-2}. Scattering through broken cloud fields enhances the diffuse radiation component relative to clear sky fluxes, a process that represents important energy input reaching the surface (e.g., Gristey et al., 2020).

Once reaching the surface, the partitioning of radiative energy into the THF components varied diurnally and as a function of sky condition. THF exchange efficiency was more effective under low stratiform compared to low cumulus; this was shown to be related to a lagged response between rapid SWD variability and the partitioning of THFs under broken cloudiness. The magnitude of median THFs, however, was three times as large for low cumulus compared to low stratiform cloud cases. This is a direct response to the efficiency of land-atmosphere

exchange driven by large net shortwave radiation. Typically, the convective mixed layer depth is intimately connected to the magnitude of the H_s, itself a function of surface moisture, surface type, and leaf area index (Tao et al., 2019). More arid land surfaces often have deeper mixed layers than wet or highly vegetated land surfaces due to large H_s compared to H_l (Lareau et al., 2018; Rabin et al., 1990). During CHEESEHEAD19, H_s during periods of clear sky and low cumulus were generally modest ranging between 50 and 150 W m^{-2}, and even lower during low stratiform cloud periods, ranging from -25 to 75 W m^{-2}. The residual surface energy was often smaller for low stratiform compared to low cumulus periods. However, the residuals for all three sky conditions examined were similar when the SEB$_{residual}$ was weighted by the available net energy at the surface, with RFD peaks around 10% with a primary range between 0% and 20%.

An important difference found from CHEESEHEAD19 compared to results from ARM SGP and from a Canadian woodland site was the partitioning amongst THFs during periods of low cumulus clouds. The THFs were dominated by H_l over northern Wisconsin, generally by a factor of three larger than H_s. The opposite was found in central Oklahoma and Canada where H_s exceeded H_l, often by a factor of two or larger (Fitzjarrald & Moore, 1994; Lareau et al., 2018; Tao et al., 2019). Such a difference suggests that the Bowen ratios over the heterogeneous, forested terrain of northern Wisconsin are markedly different from those sites. Instead, H_l was the predominant surface heat flux, typically a factor of three times larger than H_s and irrespective of cloud type. Mixed layer depths, which generally correlate with H_s, were considerably deeper during low cumulus cloud periods compared to clear sky periods despite having statistically similar ranges of H_s. Clear sky periods were most common during the morning (Zhang et al., 2017) when the growing mixed layer depth lagged the growth of the LCL during the morning transition from a more stratified to a convective boundary layer. When low cumulus periods were observed during mid-late morning, the diurnal evolution of LCL plateaued at a lower level than the LCLs when clear sky periods were observed. Constraining the LCL to lower levels is consistent with near-surface moistening (Haiden, 1997), a process that is supported by latent heat fluxes approximately 100 W m^{-2} greater during cumulus conditions compared to clear skies.

Moderate differences in near-surface meteorological conditions were observed between the cloud types at CHEESEHEAD19, suggesting locally-forced L-A interactions may have contributed to the different boundary layer evolutions (Tao et al., 2019), even potentially with feedbacks onto the cloud regime observed. Soil moisture variability, however, was similar amongst all three sky conditions examined. Variability in the partitioning of heat fluxes for a given measure of soil moisture made it difficult to assert whether soil moisture content was directly accountable for the formation and persistence of a particular sky condition; instead surface evaporation and/or evapotranspiration from the vegetation and canopy were important in partitioning the turbulent heat fluxes and promoting lower Bowen ratios. At SGP, near-surface variables like temperature and relative humidity only showed a significant correlation to boundary layer depth during peak summer months and were associated with changes in the surface leaf area index (Tao et al., 2019). The differences in near surface meteorological settings between low cumulus, low stratiform, and clear sky periods at CHEESEHEAD19 corroborate the extent of local L-A coupling. Low cumulus and clear sky periods were prone to warmer and relatively drier near-surface conditions which happened to occur more frequently during the first half of the campaign, closer to midsummer. At ARM SGP, Lareau et al. (2018) found near-surface relative humidity would decrease throughout the day and especially during the afternoon, while continually increasing near the upper third of the growing, shallow cumulus topped boundary layer. Furthermore, the study observed that profiles of absolute humidity indicated drying across the full depth of the convective boundary layer, especially after strong, negative gradients in specific humidity emerged above the shallow cumulus topped boundary layer in response to entrainment of drier air. At CHEESEHEAD19, profiles of vertical velocity variance during three low cumulus days were systematically larger than clear sky variances across the upper third of the mixed layer but below the cloud base. We hypothesize that dry air entrainment associated with the broken cloudiness enhanced the velocity variance relative to clear skies. Entrainment drying of the boundary layer is consistent with the systematically larger H_l during low cumulus periods relative to clear skies. Such a signal was not reported from multi-year profiles analyzed at ARM SGP with shallow cumulus, although Lareau et al. (2018) did observe increased vertical velocity variance and skewness compared to clear skies. This warrants further investigation across a more clear sky and low cumulus periods from CHEESEHEAD19. Future studies will use the boundary layer cloud type separation employed here to examine whether numerical weather prediction models properly represent the differences in energy partitioning observed at CHEESEHEAD19.

Conflict of Interest

The authors declare no conflicts of interest relevant to this study.

Data Availability Statement

All datasets are freely accessible from the NCAR Earth Observing Laboratory data archive, with each dataset referenced here (full citation in the References section): Surface radiation: Riihimaki et al. (2020a), Riihimaki et al. (2020b), Riihimaki et al. (2020c). Near-surface meteorology: Riihimaki et al. (2020a). Surface radiation/turbulent heat fluxes/momentum fluxes/ground heat fluxes/soil moisture: NCAR/EOL In-situ Sensing Facility (2021). Mixed layer height: Bianco and Duncan (2020); NCAR/EOL In-situ Sensing Facility (2020). Vertical velocity profiles: Wagner (2021).

References

Andrews, A. E., Kofler, J. D., Trudeau, M. E., Williams, J. C., Neff, D. H., Masarie, K. A., et al. (2014). CO2, CO, and CH4 measurements from tall towers in the NOAA Earth system Research Laboratory's Global Greenhouse gas reference network: Instrumentation, uncertainty analysis, and recommendations for future high-accuracy greenhouse gase monitoring efforts. *Atmospheric Measurement Techniques*, *7*, 647–687. https://doi.org/10.5194/amt-7-647-2014

Augustine, J. A., DeLuisi, J. J., & Long, C. N. (2000). Surfrad – A National surface radiation budget network for atmospheric Research. *Bulletin of the American Meteorological Society*, *81*(10), 2341–2358. https://doi.org/10.1175/1520-0477(2000)081<2341:SANSRB>2.3.CO;2

Berg, L. K., & Kassianov, E. I. (2008). Temporal variability of fair-weather cumulus statistics at the ACRF SGP site. *Journal of Climate*, *21*, 3344–3358. https://doi.org/10.1175/2007JCLI2266.1

Berg, L. K., Newsom, R. K., & Turner, D. D. (2017). Year-long vertical velocity statistics derived from Doppler lidar data for the continental convective boundary layer. *Journal of Applied Meteorology and Climatology*, *56*, 2441–2454. https://doi.org/10.1175/JAMC-D-16-0359.1

Bianco, L., & Duncan, J. (2020). *NOAA planetary boundary layer heights (PBLH) derived from the NOAA/PSL 915-MHz wind profiler radars. Version 1.0*. UCAR/NCAR – Earth observing Laboratory. https://doi.org/10.26023/B4RJ-38H5-C812

Bianco, L., Wilczak, J. M., & White, A. B. (2008). Convective boundary layer depth estimation from wind profilers: Statistical comparison between and automated algorithm and expert estimations. *Journal of Atmospheric and Oceanic Technology*, *25*(8), 1397–1413. https://doi.org/10.1175/2008JTECHA981.1

Brown, A. R., Cederwall, R. T., Chlond, A., Duynkerke, P. G., Golaz, J. C., Khairoutdinov, M., et al. (2002). Large-eddy simulation of the diurnal cycle of shallow cumulus convection over land. *Quarterly Journal of the Royal Meteorological Society*, *128*, 1075–1093. https://doi.org/10.1256/003590002320373210

Butterworth, B. J., Desai, A. R., Metzger, S., Townsend, P. A., Schwartz, M. D., Petty, G. W., et al. (2021). Connecting land-atmosphere interactions to surface heterogeneity in CHEESEHEAD19. *Bulletin of the American Meteorological Society*, *102*(2), E421–E445. https://doi.org/10.1175/BAMS-D-19-0346.1

Chandra, A. S., Kollias, P., Giangrande, S. E., & Klein, S. A. (2010). Long-term observations of the convective boundary layer using insect radar returns at the SGP ARM climate Research facility. *Journal of Climate*, *23*, 5699–5714. https://doi.org/10.1175/2010JCLI3395.1

Duncan, J. B., Jr., Bianco, L., Adler, B., Bell, T., Djalalova, I., Riihimaki, L., et al. (2021). Evaluating daytime planetary boundary-layer height estimations resolved by both active and passive remote sensing instruments during the CHEESEHEAD19 field campaign. *Atmospheric Measurement Techniques - Discussions*, 1–40. https://doi.org/10.5194/amt-2021-363

Ek, M. B., & Holtslag, A. A. M. (2004). Influence of soil moisture on boundary layer cloud development. *Journal of Hydrometeorology*, *5*, 86–99. https://doi.org/10.1175/1525-7541(2004)005<0086:IOSMOB>2.0.CO;2

Fast, J. D., Berg, L. K., Alexander, L., Bell, D., D'Ambro, E., Hubbe, J., et al. (2019). Overview of the HI-scale field campaign. A new perspective on shallow convective clouds. *Bulletin of the American Meteorological Society*, *100*(5), 821–840. https://doi.org/10.1175/BAMS-D-18-0030.1

Findell, K. L., & Eltahir, E. A. B. (2003). Atmospheric controls on soil moisture-boundary layer interactions. Part I: Framework development. *Journal of Hydrometeorology*, *4*, 552–569. https://doi.org/10.1175/1525-7541(2003)004<0552:ACOSML>2.0.CO;2

Fitzjarrald, D. R., & Moore, K. E. (1994). Growing season boundary layer climate and surface exchanges in a subarctic lichen woodland. *Journal of Geophysical Research*, *99*(D1), 1899–1917.

Freedman, J. M., Fitzjarrald, D. R., Moore, K. E., & Sakai, R. K. (2001). Boundary layer clouds and vegetation-atmosphere feedbacks. *Journal of Climate*, *14*, 180–197. https://doi.org/10.1175/1520-0442(2001)013<0180:BLCAVA>2.0.CO;2

Gentine, P., Entekhabi, D., Chehbouni, A., Boulet, G., & Duchemin, B. (2007). Analysis of evaporative fraction diurnal behaviour. *Agricultural and Forest Meteorology*, *143*(1–2), 13–29. https://doi.org/10.1016/j.agrformet.2006.11.002

Gentine, P., Entekhabi, D., & Polcher, J. (2011). The diurnal behavior of evaporative fraction in the soil-vegetation-atmospheric boundary layer continuum. *Journal of Hydrometeorology*, *12*, 1530–1546. https://doi.org/10.1175/2011JHM1261.1

Golaz, J.-C., Jiang, H., & Cotton, W. R. (2001). A large-eddy simulation study of cumulus clouds over land and sensitivity to soil moisture. *Atmospheric Research*, *59–60*, 373–392. https://doi.org/10.1016/S0169-8095(01)00113-2

Grachev, A. A., Fairall, C. W., Blomquist, B. W., Fernando, H. J. S., Leo, L. S., Otàrola-Bustos, S. F., et al. (2020). On the surface energy balance closure at different temporal scales. *Agricultural and Forest Meteorology*, *281*, 107823. https://doi.org/10.1016/j.agrformet.2019.107823

Gristey, J. J., Feingold, G., Glen, I. B., Schmidt, K. S., & Chen, H. (2020). Surface solar irradiance in continental shallow cumulus fields: Observations and large-eddy simulation. *Journal of the Atmospheric Sciences*, *77*, 1065–1080. https://doi.org/10.1175/JAS-D-19-0261.1

Haiden, T. (1997). An analytical study of cumulus onset. *Quarterly Journal of the Royal Meteorological Society*, *123*, 1945–1960.

Kivalov, S. N., & Fitzjarrald, D. R. (2019). Observing the whole-canopy short-term dynamic response to natural step changes in incident light: Characteristics of tropical and temperate forests. *Boundary-Layer Meteorology*, *173*, 1–52. https://doi.org/10.1007/s10546-019-00460-5

Krishnamurthy, R., Newsom, R. K., Chand, D., & Shaw, W. J. (2021). *Boundary layer Climatology at ARM southern great plains*. Technical Report 30832 – January 2021. Pacific Northwest National Laboratory. https://doi.org/10.2172/1778833

Lareau, N. P., Zhang, Y., & Klein, S. A. (2018). Observed boundary layer controls on shallow cumulus at the ARM southern great plains site. *Journal of the Atmospheric Sciences*, *75*, 2235–2255. https://doi.org/10.1175/JAS-D-17-0244.1

Lee, T. R., Buban, M., Turner, D. D., Meyers, T. P., & Baker, C. B. (2019). Evaluation of the high-resolution rapid refresh (HRRR) model using near-surface meteorological and flux observations from northern Alabama. *Weather and Forecasting*, *34*, 635–663. https://doi.org/10.1175/WAF-D-19-0184.1

Lenschow, D. H., Wyngaard, J. C., & Pennell, W. T. (1980). Mean-field and second-moment budgets in a Baroclinic, convective boundary layer. *Journal of the Atmospheric Sciences*, *37*, 1313–1326. https://doi.org/10.1175/1520-0469(1980)037<1313:MFASMB>2.0.CO;2

Long, C. N., & Ackerman, T. P. (2000). Identification of clear skies from broadband pyranometer measurements and calculation of downwelling shortwave cloud effects. *Journal of Geophysical Research*, *105*(D12), 15609–15626. https://doi.org/10.1029/2000JD900077

Long, C. N., Sabburg, J. M., Calbò, J., & Pagès, D. (2006). Retrieving cloud characteristics from ground-based daytime color all-sky images. *Journal of Atmospheric and Oceanic Technology*, *23*, 633–652. https://doi.org/10.1175/JTECH1875.1

Long, C. N., & Turner, D. D. (2008). A method for continuous estimation of clear-sky downwelling longwave radiative flux developed using ARM surface measurements. *Journal of Geophysical Research*, *113*, D18208. https://doi.org/10.1029/2008JD009936

McNicholas, C., & Turner, D. D. (2014). Characterizing the convective boundar layer turbulence with a high spectral resolution lidar. *Journal of Geophysical Research: Atmospheres*, *119*, 12910–12927. https://doi.org/10.1002/2014JD021867

Milovac, J., Warrach-Sagi, K., Behrendt, A., Späth, F., Ingwersen, J., & Wulfmeyer, V. (2016). Investigation of PBL schemes combining wht WRF model simulations with scanning water vapor differential absorption lidar measurements. *Journal of Geophysical Research: Atmospheres*, *121*, 624–649. https://doi.org/10.1002/2015JD023927

NCAR/EOL In-situ Sensing Facility. (2020). *NCAR/EOL ISS ceilometer data. Version 1.0*. UCAR/NCAR – Earth observing Laboratory. https://doi.org/10.26023/W3XH-2KYX-2C01

NCAR/EOL In-situ Sensing Facility. (2021). *NCAR/EOL 5 minute ISFS surface flux data, tilt corrected, geographic coordinate winds. Version 2.1*. UCAR/NCAR – Earth Observing Laboratory. https://doi.org/10.26023/43MF-NP8N-3Q0V

Rabin, R. M., Stadler, S., Wetzel, P. J., Stensrud, D. J., & Gregory, M. (1990). Observed effects of landscape variability on convective clouds. *Bulletin of the American Meteorological Society*, *71*(3), 272–280.

Ramanathan, V., Cess, R. D., Harrison, E. F., Minnis, P., Barkstrom, B. R., Ahmad, E., & Hartmann, D. (1989). Cloud-radiative forcing and climate: Results from the Earth radiation budget experiment. *Science*, *243*(4887), 57–63. https://doi.org/10.1126/science.243.4887.57

Rieck, M., Hohenegger, C., & van Heerwaarden, C. C. (2014). The influence of land surface heterogeneities on cloud size development. *Monthly Weather Review*, *142*, 3830–3846. https://doi.org/10.1175/MWR-D-13-00354.1

Riihimaki, L., Lantz, K., & Sedlar, J. (2020a). *NOAA/GML SURFRAD RadFlux analysis products (radiation and cloud), ISS site Version 1.0*. UCAR/NCAR – Earth Observing Laboratory. https://doi.org/10.26023/EPE7-FWXN-CD0M

Riihimaki, L., Lantz, K., & Sedlar, J. (2020b). *NOAA/GML SURFRAD RadFlux analysis products (radiation and cloud), ARV Lakeland site. Version 1.0*. UCAR/NCAR – Earth observing Laboratory. https://doi.org/10.26023/R48S-CJDC-JS0D

Riihimaki, L., Lantz, K., & Sedlar, J. (2020c). *NOAA/GML SURFRAD RadFlux analysis products (radiation and cloud). PRW Prentice Site. Version 1.0*. UCAR/NCAR – Earth Observing Laboratory. https://doi.org/10.26023/76TC-GYJV-DT06

Santanello, J. A., Jr., Dirmeyer, P. A., Ferguson, C. R., Findell, K. L., Tawfik, A. B., Berg, A., et al. (2018). Land-atmosphere interactions. The LoCo perspective. *Bulletin of the American Meteorological Society*, *99*(6), 1253–1272. https://doi.org/10.1175/BAMS-D-17-0001.1

Santanello, J. A., Jr., Peters-Lidard, C. D., & Kumar, S. V. (2011). Diagnosing the sensitivity of local land-atmosphere coupling via the soil moisutre-boundary layer interaction. *Journal of Hydrometeorology*, *12*, 766–786. https://doi.org/10.1175/JHM-D-10-05014.1

Sedlar, J., Riihimaki, L. D., Lantz, K. D., & Turner, D. D. (2021). Development of a random-forest cloud-regime classificaiton model based on surface radiation and cloud products. *Journal of Applied Meteorology and Climatology*, *60*, 477–491. https://doi.org/10.1175/JAMC-D-20-0153.1

Sisterson, D. L., Peppler, R. A., Cress, T. S., Lamb, P. J., & Turner, D. D. (2016). The AR southern great plains (SGP) site. *Meteorological Monographs*, *57*, 6–16. https://doi.org/10.1175/AMSMONOGRAPHS-D-16-0004.1

Stull, R. B. (1988). *An introduction to boundary layer meteorology*. Kluwer Academic Publishers.

Tao, C., Zhang, Y., Tang, S., Tang, Q., Ma, H.-Y., Xie, S., & Zhang, M. (2019). Coupling over the U.S. Southern great plains inferred from the ARM long-term observations. *Journal of Geophysical Research: Atmospheres*, *124*, 10091–10108. https://doi.org/10.1029/2019JD030585

Turner, D. D., Vulfmeyer, V., Berg, L. K., & Schween, J. H. (2014). Water vapor turbulence profiles in stationary continental convective mixed layers. *Journal of Geophysical Research: Atmospheres*, *119*, 11151–11165. https://doi.org/10.1002/2014JD022202

van Driel, R., & Jonker, H. J. J. (2011). Convective boundary layers driven by nonstationary surface heat fluxes. *Journal of the Atmospheric Sciences*, *68*, 727–738. https://doi.org/10.1175/2010JAS3643.1

Wagner, T. (2021). *SSEC SPARC Doppler LiDAR at WLEF. Version 1.0*. UCAR/NCAR – Earth Observing Laboratory. https://doi.org/10.26023/J41B-5NH1-840B

Xiao, H., Berg, L. K., & Huang, M. (2018). The impact of surface heterogeneities and land-atmosphere interactions on shallow clouds over ARM SGP site. *Journal of Advances in Modeling Earth Systems*, *10*, 1220–1244. https://doi.org/10.1029/2018MS001286

Zhang, Y., Klein, S. A., Fan, J., Chandra, A. S., Kollias, P., Xie, S., & Tang, S. (2017). Large-eddy simulation of shallow cumulus over land: A composite case based on ARM long-term observations at its southern great plains site. *Journal of the Atmospheric Sciences*, *74*, 3229–3251. https://doi.org/10.1175/JAS-D-16-0317.1

Zhong, S., & Doran, J. C. (1997). A study of the effects of spatially varying fluxes on cloud formation and boundary layer properties using data from the southern great Pleains cloud and radiation testbed. *Journal of Climate*, *10*, 327–341. https://doi.org/10.1175/1520-0042(1997)010<0327:ASOTEO>2.0.CO;2

Zhou, B., Sun, S., Sun, J., & Zhu, K. (2019). The universality of the normalized vertical velocity variance in contrast to the horizontal velocity variance in the convective boundary layer. *Journal of the Atmospheric Sciences*, *76*, 1437–1456. https://doi.org/10.1175/JAS-D-18-0325.1